AN INNOVATIVE CLOSED FRACTURE ACIDIZING TECHNIQUE FOR DEEP CARBONATE RESERVOIRS USING GLDA

A Dissertation

by

JIA HE

Submitted to the Office of Graduate and Professional Studies of
Texas A&M University
in partial fulfillment of the requirements for the degree of

DOCTOR OF PHILOSOPHY

Chair of Committee,	Hisham Nasr-El-Din
Committee Members,	Ding Zhu
	Maria A. Barrufet
	Mahmoud M. El-Halwagi
Head of Department,	A. Daniel Hill

August 2015

Major Subject: Petroleum Engineering

Copyright 2015 Jia He

ABSTRACT

The closed fracture acidizing (CFA) technique is designed to overcome inadequate conductivity development in traditional acid fracturing treatments. However, achieving adequate fracture length is challenging due to the fast acid spending rates and the high corrosion rate to well tubular, especially at high temperatures. This study developed a new closed fracture acidizing (CFA) technique using glutamic acid-N,N-diacetic acid (GLDA) to overcome the limitations of conventional acid fracturing systems and achieve significant length and final fracture conductivity.

In this study, a tensile fracture was created across a low permeability Indiana limestone core of 6 in. in length and 1.5 in. in diameter, using an Instron electric compression test machine. The rough fracture surfaces created were scanned using a profilometer to characterize the etched fracture faces before and after the CFA tests. CFA tests were then conducted using a specially designed coreflood setup with the injection of 20 wt% GLDA and 15 wt% HCl at various temperature conditions. CT scans were used to characterize the grooves or channels developed in the CFA tests. The concentrations of the dissolved calcium ions were measured using Inductively Coupled Plasma–Optical Emission Spectroscopy (ICP-OES), and the effluent samples were titrated to determine the acid concentration.

Results show that closed fractures substantially increased the core permeability under low closure stress, with limited increase under high closure stress (>1,500 psi). Surface topography of natural tensile fractures was highly correlated with initial

permeability of tensile fractures and had little correlation with the changing rate of fracture permeability with closure stress; while rock embedment strength was found to be mostly associated with permeability change. 20 wt% GLDA was effective in creating a sufficient amount of flow channels to obtain substantial fracture conductivity at various closure stress conditions. Rock embedment strength measurements showed that 15% HCl tends to weaken the rock embedment strength by more than 20%, while 20 wt% GLDA weakens the rock embedment strengthen by no more than 13% on average. Under all circumstances, most of the HCl was consumed after being injected across the cores, thus resulting in limited fracture length in field conditions.

DEDICATION

To my wife, Jie Xiao, my parents, and my family for their love, encouragement, and support

ACKNOWLEDGEMENTS

I would like to thank my committee chair, Dr. Hisham Nasr-El-Din, for his support, supervision, and assistance in this work. Thanks also go to my three committee members, Dr. Ding Zhu, Dr. Maria A. Baffufet, and Dr. Mahmoud M. El-Halwagi, for their cooperation and support.

Also I am grateful for my friends and colleagues and the department faculty and staff for making my time at Texas A&M University a great experience. I also want to extend my gratitude to AkzoNobel for supporting this project.

I greatly acknowledge McNew Research Laboratory for granting permission to utilize the load frame for fracturing cores, Digital Surf for the free trial of the topography software, and the Petroleum Engineering Department at Texas A&M University for their research facilities.

NOMENCLATURE

PVbt	Pore volume to breakthrough
CFA	Closed fracture acidizing
c_1	Initial fracture permeability prior to any closure stress, darcies
c_2	Rate of fracture permeability change with closure stress, psi^{-1}
d	Diameter of intact cores, in.
d_i	Diameter of the steel ball, in.
$k_{effective}$	Permeability of fractured cores, md
k_f	Permeability of tensile fracture, md
k_m	Permeability of intact cores (matrix permeability), md
p_c	The closure stress, psi
RES	Rock embedment strength, psi
W	Applied load, lbf
w_f	Tensile fracture width, μm
ϕ_f	Tensile fracture porosity

TABLE OF CONTENTS

Page

LIST OF FIGURES

Page

LIST OF TABLES

Page

1. INTRODUCTION

The Closed Fracture Acidizing (CFA) technique was firstly developed in the 1980s. It is applicable where traditional acid fracturing is not successful in creating and maintaining high fracture conductivity, such as uniform dissolution of fracture face, crushed fracture face by high closure stress, or low solubility in acid. This technique involves injection of acid across a closed fracture plane to create wormholes or flow channels that can maintain extreme high fracture conductivity over a wide range of closure stress conditions. The closed fractures can be natural or hydraulic fractured, and the factors that cause fractures to close can be due to geological factors or incompatible fluids.

However, the documented application of CFA mainly has been used as a final stage following tradition acid fracturing treatments. Few studies have been involved the investigation of CFA as a separate treatment in closed natural fractures or closed hydraulic fractures. Besides, the traditional acid systems used in acid fracturing are mostly HCl-based. It is very challenging to achieve enough fracture length due to the high acid reaction rate, high leakoff rate and high corrosion rate. In this study, a new chelate, glutamic acid N,N-diacetic acid (GLDA), is tested to treat closed fractures. This chelate has been successfully used in matrix acidizing high temperature formations. It is thermally stable and environmental friendly.

The objective of this study will demonstrate the applicability of GLDA as standalone closed fracture acidizing fluids in deep, naturally fractured carbonate

reservoirs. Extensive laboratory studies, including etch patterns, acid/wormhole propagation velocity, conductivity measurements, and rock strength measurement will be conducted to examine the effectiveness of this new acid fracturing technique. The following objectives will be accomplished in this study:

(1) Statistically investigate the effect of closure stress on properties of natural tensile fractures and provide a method to predict fracture permeability by focusing on the characterization of the surface topography of natural fractures;

(2) Characterize the etching patterns of 20 wt% GLDA over a wide range of temperatures and compare with those etched with 15 wt% HCl;

(3) Determine the optimal conditions of 20 wt% GLDA as a standard alone fluid to closed fracture acidizing deep limestone formation;

(4) Investigate the mechanisms of CFA by 20 wt% GLDA and 15 wt% HCl.

2. LITERATURE REVIEW

2.1 Closure Behavior of Fractures

In the petroleum industry, more than 50% of oil and gas is produced from naturally fractured reservoirs (Duan et al. 2000). The closure behavior of natural fractures has been widely investigated due to its importance to reservoir productivity and recovery factor, especially to unconventional reservoirs nowadays. Natural fractures in an unconventional reservoir rapidly shrink with an increase of effective stress and will result in significant long-term loss in productivity (Aybar et al. 2014; Ozkan et al. 2010; Patzek et al. 2013; Torcuk et al. 2013; Sarna et al. 2014).

The fracture permeability and its variation with confining pressure, fluid pressure and tectonic stresses has been studied both experimentally (Iwai 1976; Gale 1977; Trimmer et al. 1980; Kranz 1979; Jaeger and Cook 1979) and theoretically (Tsang and Witherspoon 1981; Gavrilenko and Gueguen 1989; Chacon and Tiab 2007). Studies show that closure of natural fractures is affected by many factors such as closure stress, rock properties, fracture properties, initial aperture, and topographies of fracture surfaces. Apertures of natural fractures are found to be very sensitive to the applied closure stress (Vega Navarro 2012). Their sensitivity to applied closure stresses are mainly due to two factors: decrease of fracture apertures and increased number of contact points and area under higher compressive stresses. These two factors will reduce the cross section of flow area and increase the resistance to flow because of an induced longer and more tortuous fluid path (Walsh 1981; Vega Navarro 2012). The other

factors, e.g., rock properties and fracture properties (Van Dam et al. 2000; Van Dam et al. 2002; Duan et al. 2000; Kranzz et al. 1979) are also discussed in details.

Surface topography was firstly used by Ruffet el al. in 1998 to investigate the relation between surface topography and acid fracture conductivity. They concluded that residual conductivity of an acid fracture depends on the roughness of the faces in contact and that the roughness depends on the initial etching topography and asperities deformation (Rodrigues et al. 2011). Since then, surface characterization of acid fracture has been considered to be an effective tool to predict acid conductivity of acid fracture (Nieto et al. 2007; Pournik et al. 2007; Antelo et al. 2009). In natural fractures, surface topography was also considered to be an important factor affecting the fracture permeability (Cho et al. 2013). However, few studies have been conducted on how to predict fracture permeability or fracture conductivity by incorporating surface topography knowledge.

2.2 Closed Fracture Acidizing

Closed Fracture Acidizing (CFA) technique was firstly developed in the 1980s to overcome some drawbacks of conventional acid fracturing treatments, such as inadequate conductivity development in the fracture length or loss of conductivity at high closure stress conditions (Fredrickson 1986). The basic concept of this technique is to inject acid at low rates below formation fracturing pressure into a well with closed fractures. The fractures can be natural, hydraulically fractured or acid fractured prior to CFA treatment (Knox and Fredrickson 1973, 1974; Broaddus and Fredrickson 1975).

During the treatment, acid preferentially flows the areas with least flow resistance developed by closed fracture networks and creates wormholes or flow channels across the fracture plane with much higher conductivity and greater strength than conventional fracture acidizing. This allows deep acid penetration and stable fracture conductivity under high closure stress conditions. CFA can be used in many conditions including uniformly dissolved fracture face by acid to prevent well defined flow channels, crushed well defined-grooves at high closure stress, or low solubility of formation in acid resulting in low fracture conductivity.

Fredrickson (1986) documented the early development of CFA treatment based on both laboratory studies and field applications. Fracture flow capacity was found to be in excess of 100,000 md-ft in most of the laboratory tests. Excellent field results by more than 6 fold increase can be achieved through CFA. However, he stated that CFA can be a viable option but will not work on all formations. The typical acid etching time of closed fractures was specified at 18, 36, and 54 mins for experimental studies. Anderson and Fredrickson (1989) proposed a new laboratory procedure for dynamic acid etching tests to evaluate and optimize acid fracturing treatments. Conventional acid fracturing treatments maintained very low fracture conductivity at high closure stress as a result of crushed etched faces; while CFA produced adequate conductivities that were much less susceptible to high closure stress. Most of the tests applied 18 and 54 mins of acid etching time. Through well test analysis, Sliman et al. (1990) stated that fracture conductivity following a CFA treatment was more than 100,000 md-ft. The fluid flow model was characterized by closed fractures with relatively low conductivity and highly

conductive wormholes by acid etching. In Lisburne Field of Prudhoe Bay, conventional acid fracturing with gelled 28% HCl and proppant hydraulic fracturing both resulted in high initial production rates but with sharp decline to pre-stimulation rates. Successful application of CFA using emulsified acid achieved sustained high production rates (Bartko et al. 1992). Several recent field applications of CFA have demonstrated the increased fracture conductivity or improvement in production rates, compared with conventional acid fracturing treatments (Sizer et al. 1991; Wang et al. 2003; Garzon et al. 2008; Nasr-El-Din et al. 2009; Inda et al. 2009). Pournik et al. (2011) proposed a new experimental set-up to perform CFA tests on already acid fractured cores. Experimental results showed that higher fracture conductivity was obtained with lower polymer concentration and leakoff allowance.

2.3 Acid Systems

Acid fracturing techniques are the primary stimulation preference for carbonate reservoirs (Abass et al., 2006; Al-Omair et al. 2008). It is less complicated because no proppants are used. There is no risk of premature screen-out, which can leave the fracturing tubing string full of proppant (Cleary et al. 1993; Aud et al. 1994). There are no problems of proppant flowback, proppant embedment damage, and cleanout from the wellbore (Van Batenburg et al. 1999; Raysoni and Weaver 2012; Liu et al. 2003). In deep carbonate reservoirs, the permeability is low, but natural fractures are usually present (Nnanna and Ajienka 2005; Abass et al. 2007; Jahediesfanjani and Civan 2006). Propped fracturing is not preferred in naturally fractured carbonate reservoirs because it

is difficult to place enough proppant in the fracture geometry with tortuous paths and complex stress properties (Kalfayan 2008).

The success of acid fracturing mostly depends on the etched fracture conductivity and acid penetration distance. According to Nierode and Kruk (1973), acid etched fracture conductivity is based on the volume of rock dissolved and the rock mechanical strength. Rock mechanical strength tends to be weakened by acid (Beg et al. 1998; Gong et al. 1999; Melendez et al. 2007), and acid-system choices make a significant difference in the degree of rock softening of carbonates (Nasr-El-Din et al. 2009). The rock strength and closure pressure must indicate that good conductivity will remain after fracture closure. Acid penetration distance is a function of acid type, leak-off rate, fracture width, pumping rate and volume (Bartko et al. 1992). The rock heterogeneity also plays an important role in determining acid fracture conductivity. Among all the factors, acid system choice significantly influences resulting fracture conductivity because it determines the degree of etching, the etching pattern, rock embedment strength softening due to differences in chemical and physical properties (Pournik et al. 2007, 2010a, 2010b; Pournik and Nasr-El-Din 2010).

Traditionally, 28 wt% HCl was used in low carbon steel tubular, including regular acid, emulsified acid (Nasr-El-Din et al. 2001), in-situ gelled acid (Lynn and Nasr-El-Din 2001), and viscoelastic surfactant-based acid (Nasr-El-Din et al. 2003; 2006a). 15 wt% HCl – 9 wt% formic acid was used to stimulate wells completed with super Cr-13 tubing (Nasr-El-Din et al. 2002a, 2006b). Those acid systems resulted in high initial production rates but some decreased to less than 60% of original production

rates within six months of production (Bartko et al. 2003). Synthetic polymers in gelled acids were used to control leak-off but a possibility of formation damage may occur, especially in tight formations (Taylor and Nasr-El-Din 2001, 2002; Nasr-El-Din et al. 2002b). The presence of viscoelastic surfactants and acid-soluble polymers can alleviate the high leakoff rate to some extent, but large volumes of acid are still need to create an effectively etched fracture length (Nasr-El-Din et al. 2009). Overall, achieving adequate fracture length using HCl-based systems is challenging due to the fast acid spending rates. In addition, concentrated HCl-based acids are very corrosive to well tubular, especially at high temperatures.

To overcome problems associated with strong acids, L-glutamic acid diacetic acid (GLDA), a newly developed environmentally friendly chelate, has been examined as a replacement for or in combination with acid treatments in deep carbonate reservoirs (LePage et al. 2011). Experimental studies indicated that GLDA has a very good ability to dissolve calcite from carbonate rocks over a wide pH range by using a combination of acid dissolution and chelation (Rabie et al 2011). A unique property of GLDA is its high solubility; solutions exceeding 40 wt% can be achieved at a pH of approximately 2. Throughout the pH range, GLDA appears to be thermally stable up to 350°F. From an environmental standpoint, GLDA is readily biodegradable (Mahmoud et al. 2011a; 2011b). As a replacement for HCl acid, GLDA is significantly safer and less corrosive.

2.4 Importance

In all the literature studies, the successful application of CFA was mainly as a final matrix acidizing stage following viscous fingering treatments or conventional viscous acid fracturing treatments. Regular 15 wt% or 28 wt% HCl and HCl/organic acid blends are most commonly used as the CFA treatment fluid. However, the CFA technique can also be used as a single treatment procedure in naturally or propped fractured formations (Kalfayan 2008).

In this study, the closure behaviors of natural fractures will be examined based on detailed analysis of surface topography of natural fractures. Various well-defined surface parameters by ISO standards will be used to correlate with fracture permeability under different closure stress conditions. This study will statistically investigate the effect of closure stress on properties of natural tensile fractures and provide a method to predict fracture permeability by focusing on the characterization of the surface topography of natural fractures.

This study will also demonstrate the applicability of GLDA as a standalone acid fracturing fluids in deep, naturally fractured carbonate reservoirs. Extensive laboratory studies, including etch patterns, acid/wormhole propagation velocity, conductivity measurements, and rock strength measurement will be conducted to examine the effective of this new acid fracturing technique. The optimal application condition of 20 wt% GLDA as a standalone closed fracture acidizing fluid will be determined.

3. EXPERIMENTAL METHODS AND SET-UP

3.1 Experimental Studies

Low permeability Indiana limestone core samples (1.5 in. × 6 in.) with an average porosity of 20 % and permeability of 5 md were used. All cores were dried at 100˚C for 4 hours, weighed, and then saturated with deionized water to calculate the pore volume and porosity of the cores. Deionized water with a resistivity of 18.2 MΩ·cm at 77°F was used to dilute the original GLDA solution to 20 wt%. The original GLDA solution was received from AkzonNobel, and a sample of approximately 300 ml was taken for fluid analysis **(Table 1).** Hydrochloric acid at 15 wt% was prepared in the same deionized water through dilution of 36.46 wt% HCl, which was obtained from Mallinckrodt Chemical Inc. and 0.5 vol% corrosion inhibitor, was added to 15 wt% HCl.

Table 1—Summary of fluid analysis for original GLDA solution.

Parameter	**Value**
Formula	GLDAH3Na
pH	3.89
Density, g/cm3	1.26
Concentration, wt%	37.2%
Kinematic viscosity, mm2/s	6.95

* All were measured at room temperature.

3.2 Core Preparation

Indiana limestone core samples (1.5 in. × 6 in.) were fractured into two halves using the instron electric compression test machine shown in **Fig. 1.** The load frame will be stopped automatically whenever there is a main fracture developed across the 6 in. low permeability Indiana limestone. During the test, the compressive load and compressive extension were recorded, and the Young's modulus was calculated automatically at the end of each test. Next, the corners of two core halves were covered with silicone rubber and core surfaces were sealed using Teflon shrinkable tubing to prevent any bypass of the acid around the sides of the core samples. Subsequently, the cores were saturated with deionized water for 12 hours.

Fig. 1—Instron electric compression test machine.

3.3 Core Flood Set-Up

The core flood setup consisted of a syringe pump, a core holder connected to three separate cylinders supplying for acid, deionized water and seawater, a pressure transducer measuring the pressure drop across the core, a pump to apply an overburden pressure over the rubber sleeve containing the core sample, a regulator system, and a fraction collector. A schematic of the core flood set-up is shown in **Fig. 2.** The core holder is a special designed pressure tapped core holder manufactured by Core Lab Inc., and it allows measurements of the pressure drop along the length of core sample during the test. Besides, the pressure taps can be used to simulate the leakoff conditions in the field.

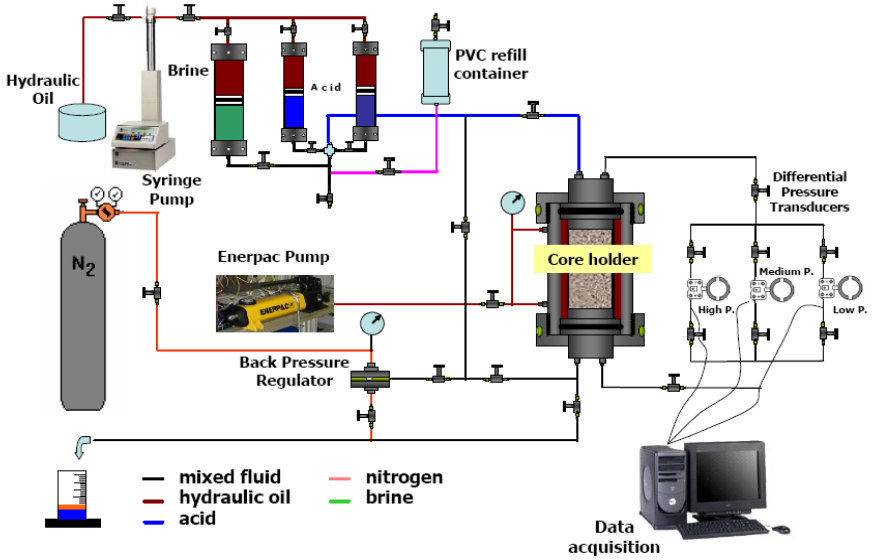

Fig. 2—Core flooding set-up.

3.4 Surface Characterization

A profilometer was used to characterize fracture rough surfaces before and after core flood test **(Fig. 3).** The vertical measurement was made using a laser displacement sensor, while the sample was moved along its length and width on a moving table. All the experiments used a 0.05 in. measurement interval in the x and y direction. The resolution on the vertical measurement was 0.002 in.; while in the horizontal directions, the transducer resolution was 0.00008 in.

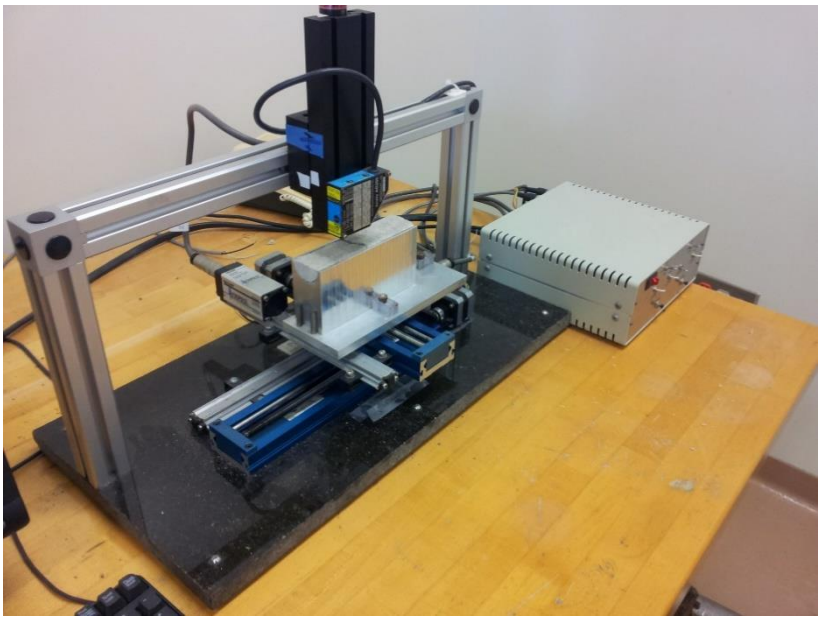

Fig. 3—Surface laser profilometer.

3.5 Rock Embedment Strength Measurements

An Instron electric compression test machine shown in Fig. 1 was used to determine the rock embedment strength before and after acid injection. The test procedure for determining the embedment pressure of the rock was proposed by Howard and Fast in 1970. In this method, a steel ball was used to indent the surface of the rock and then the embedment pressure was calculated based on the applied load and the projected area **(Eq. 1).** A steel ball with a diameter of 0.177 in. was used in this study, and the indentation distance was specified at around 0.01 in.

$$S_{RE} = \frac{W(lbs)}{\frac{\pi d_i^{\,2}}{4}(in^2)} \tag{1}$$

3.6 Experimental Procedures

Once the core samples were well prepared, they were loaded into the core holder and acidized with 20 wt% GLDA and 15 wt% HCl, respectively, until acid breakthrough. The cores were scanned using the profilometer to characterize the rough surfaces before and after the CFA tests and CT scanned to characterize any grooves or channels developed during the CFA test. The concentrations of the dissolved calcium ions were measured using Inductively Coupled Plasma–Optical Emission Spectroscopy (ICP-OES), and the effluent samples were titrated to determine the acid concentration. Rock embedment strengths were measured before and after the CFA tests. Permeability of the fracture cores and intact cores were measured to examine the effect of tensile fractures on core permeability under different closure stress conditions. A commercial

topography software was used for fracture surface analysis, and the experimental parameters are then correlated to determine the most important factors affecting the CFA process.

4. CLOSURE BEHAVIORS OF FRACTURED CORES

4.1 Characterization of Fractured Cores

Fig. 4 shows the relationship between the compressive load and the compressive extension in a typical loading test. When a main fracture was created across the 6 in. low permeability Indiana limestone, the loading frame was stopped automatically, and the breaking point was found to be at 0.02592 in. in this case. Thirty-three core samples were used for statistical analysis to generate a more representative data set.

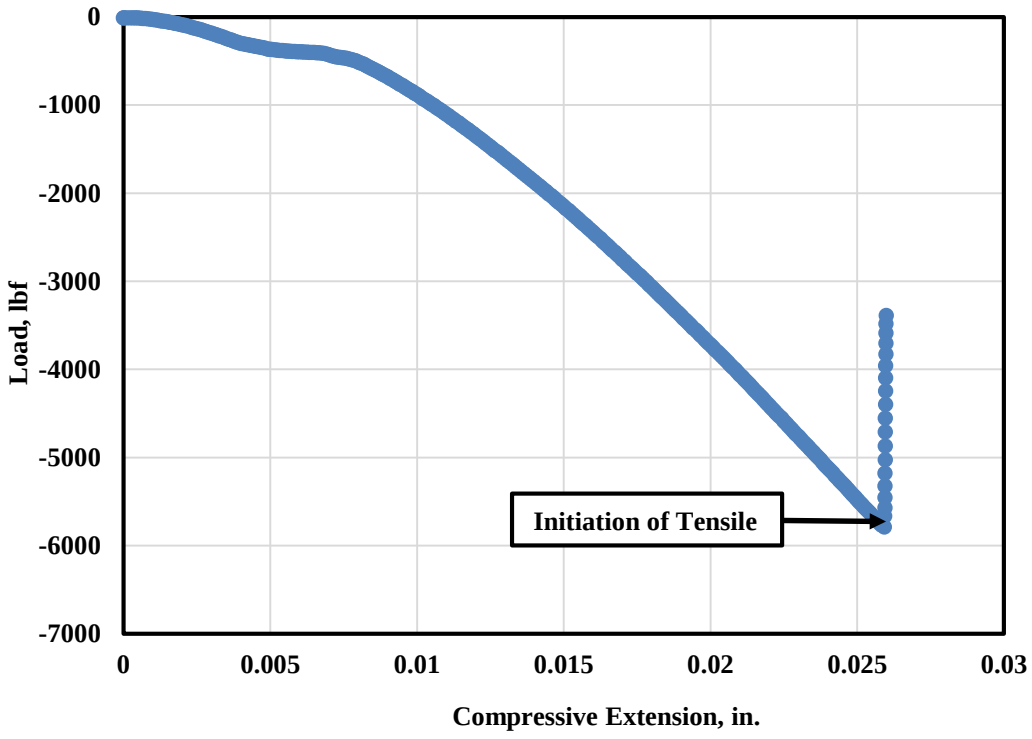

Fig. 4—Compressive extension as a function of compressive load.

The maximum compressive load, the compressive extension at maximum load, and the Young's modulus of all the core samples were recorded during each loading test. All of the core data is summarized in **Table 2**. The permeability of the cores ranged from 5 to 12 md among the 33 samples. Statistical analysis showed that, during the generation of tensile fractures, the maximum compressive load ranged from 3,836 to 7,487 lbf and had an average value of approximately 5,905 lbf. The Young's modulus ranged from 14 to 27 ksi and had an average value of approximately 21 ksi. The compressive extensions at the maximum load were from 0.02592 to 0.11792 in. with an average value of approximately 0.04455 in. The values of the rock embedment strength ranged from 15,022 to 40,645 psi with an average value of 27,247 psi. These values show that low permeability Indiana limestone cores are relatively homogeneous in terms of mechanical properties. Any steel indentation on the core surface can affect fluid flow across the fracture faces. Therefore, 10 indentation points evenly distributed across the length direction of tensile fracture surfaces were selected for embedment strength measurements. Then, the values were averaged to be the rock embedment strength for each core sample.

Table 2—Properties of un-fractured cores.

Core #	Pore Volume, cm^3	Absolute Permeability, md	Compressive Load at Maximum Load, lbf	Compressive Extension at Maximum Load, in.	Young's Modulus, ksi	Rock Embedment Strength, psi
3	23.8	8.7	3,836.1	0.04650	18.2	22,196
4	24.7	6.6	7,486.6	0.03234	26.3	21,220
5	25.0	5.4	6,172.9	0.05017	23.8	17,622
6	25.0	6.8	5,160.0	0.04197	20.7	23,890
8	26.9	9.6	5,169.4	0.03041	22.9	34,377
9	25.9	8.9	5,791.9	0.05723	23.6	30,357
10	25.4	7.2	5,895.9	0.05241	21.0	27,492
11	24.9	8.3	6,787.6	0.03846	14.1	31,661
12	23.8	6.4	5,789.0	0.02592	25.2	19,597
13	24.1	6	6,260.9	0.02949	27.2	28,697
15	23.6	5.1	6,377.0	0.03015	23.1	24,032
17	24.9	5.4	5,316.6	0.03650	20.1	31,411
18	23.8	5.2	5,811.9	0.11792	20.1	33,110
19	25.2	5.8	6,528.5	0.03100	24.9	39,761
20	18.5	5.8	6,045.1	0.03208	24.7	17,606
21	20.9	5.6	6,120.8	0.03733	17.7	38,574
22	27.7	5.8	5,477.1	0.02898	21.5	29,088
23	25.7	6.5	5,940.6	0.05259	20.8	30,210
26	26.9	11.2	6,403.9	0.04741	18.3	30,886
27	30.8	6.1	6,598.9	0.04909	19.3	23,032
28	26.0	7.8	5,476.6	0.04725	19.8	31,661
29	25.3	5.8	5,871.4	0.04012	22.0	39,015

Table 2. continued

Core #	Pore Volume, cm^3	Absolute Permeability, md	Compressive Load at Maximum Load, lbf	Compressive Extension at Maximum Load, in.	Young's Modulus, ksi	Rock Embedment Strength, psi
30	25.7	6.7	6,164.5	0.03383	22.2	17,359
31	24.4	6	5,825.1	0.04012	20.8	18,659
32	25.6	7.6	4,286.8	0.03833	21.5	24,523
33	19.1	6.2	5,498.0	0.03009	21.3	30,661
34	21.5	7.4	6,735.5	0.05250	26.1	30,661
35	24.5	4.9	6,900.6	0.05700	20.3	17,477
36	24.6	7.1	6,073.0	0.05127	22.3	40,645
37	22.3	6.6	4,191.7	0.05245	19.3	15,022
38	19.1	6.5	6,193.8	0.05414	19.1	23,287
39	24.2	10.9	5,964.1	0.05475	17.9	28,110
40	25.9	6.5	6,718.3	0.05030	21.2	27,262

The fracture faces were then scanned using the profilometer. A typical 3D fracture contour plot of Core #12A in **Fig. 5** shows a rather rough surface. In the field, fractures are mainly tensile or shear induced and tend to be naturally rough. Tensile fractures without horizontal or vertical displacements were examined in this study. Therefore, rough fracture faces created by the loading frame are more representative of actual field conditions. The rough surface can affect the dynamics of the fluid flow across the core as well as the mechanical properties of the tensile fracture faces. The aim of this study was to examine the most important factors that can contribute to fracture conductivity through permeability measurements and fracture face characterizations, and

thus provide insights on how to effectively predict the effect of closure stress on fracture permeability.

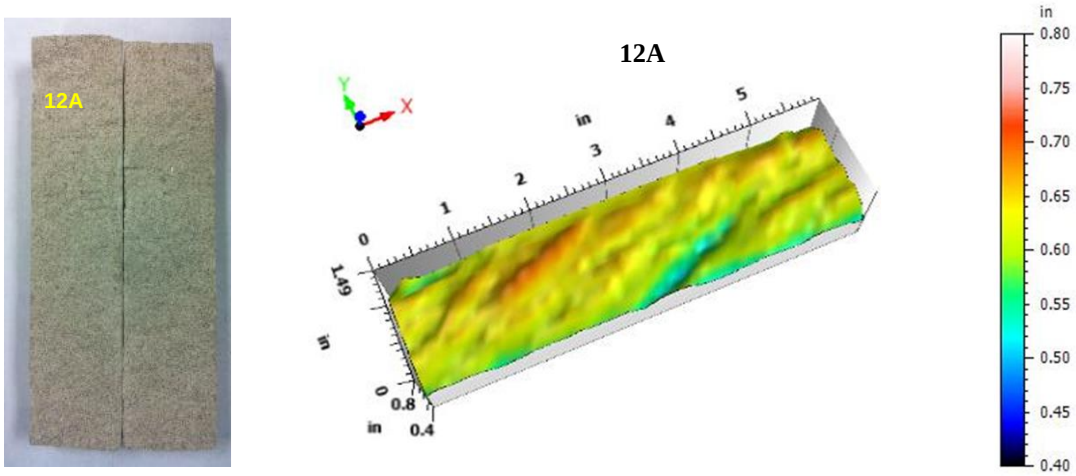

Fig. 5—3D contour plot of Core #12A.

After the rough fracture faces were scanned using a profilometer, the two core halves were put together and then sealed with silicone rubber and shrinkable Telfon tubing to prevent any bypass of fluid flow around the corners of the cores. Permeability of the fractured cores shown in **Table 3,** were measured at pressures up to 1,500 psi. **Fig. 6** shows that the closure stress has a limited effect on the intact core permeability at pressures below 1,000 psi and no effect at all at pressures above 1,000 psi. If the cores were fractured using the loading machine, the closed fracture substantially increased the core permeability up to 140.3 md under closure stress of 300 psi with a limited increase

under 1,500 psi. With the increment of closure stress, more asperities of the tensile fractures were closed and fluid flow pathways were restricted, resulting in a sharp decrease from 140.3 to 18.2 md of the permeability of fractured cores.

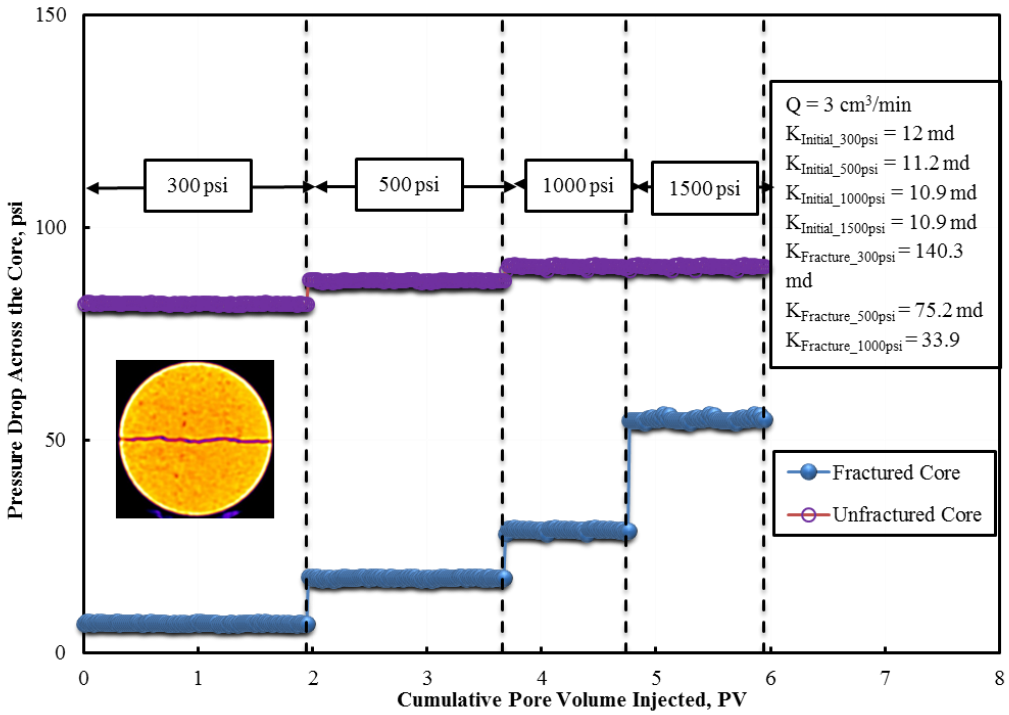

Fig. 6—Permeability of unfractured and fractured Core #39 under different closure stress conditions.

Table 3—Permeability of fractured cores at different closure stresses.

Core #	Permeability at Different Closure Stress, md				Initial Permeability, md
	300 psi	500 psi	1,000 psi	1,500 psi	
3	140.3	49.1	21.8	12.3	8.7
4	165.3	60.3	12.0	9.8	6.6
5	190.7	40.2	19.8	7.8	5.4
6	180.6	43.2	22.1	11.2	6.8
8	140.0	56.2	26.4	18.2	9.6
9	122.0	44.6	36.2	15.3	8.9
10	140.3	46.8	26.5	12.3	7.2
11	98.2	49.1	23.4	14.2	8.3
12	70.2	44.2	10.9	8.1	6.4
13	115.6	54.8	22.3	11.2	6.0
15	120.0	48.2	23.0	7.8	5.1
17	96.7	44.6	28.0	12.4	5.4
18	19.3	13.1	8.0	6.3	5.2
19	46.8	31.9	20.1	16.4	5.8
20	233.8	62.7	10.9	7.1	5.8
21	54.6	45.2	16.8	12.4	5.6
22	48.5	28.4	10.9	8.0	5.8
23	18.2	11.7	8.0	7.4	6.5
26	109.1	81.9	30.5	21.1	11.2
27	131.0	87.3	16.4	10.6	6.1

Table 3. continued

Core #	Permeability at Different Closure Stress, md				Initial Permeability, md
	300 psi	500 psi	1,000 psi	1,500 psi	
28	56.9	38.5	14.6	11.7	7.8
29	261.9	169.1	65.5	50.4	5.8
30	180.2	56.3	16.7	8.2	6.7
31	142.3	39.3	12.5	7.0	6.0
32	110.8	40.2	28.5	9.8	7.6
33	163.7	122.8	44.6	17.9	6.2
34	93.5	46.8	19.0	13.4	7.4
35	327.4	272.8	29.2	16.4	4.9
36	35.8	24.3	17.6	12.6	7.1
37	245.6	70.2	11.6	8.2	6.6
38	37.2	20.5	8.9	7.8	6.5
39	140.3	75.2	33.9	18.2	10.9
40	81.9	44.6	16.6	11.7	6.5

4.2 Properties of Tensile Fractures

As indicated above, the two important characteristics of generated tensile fracture are highly dependent on closure stress and rough faces with varied asperities. The objective of this section is to quantify the properties of the tensile fractures under different closure stress conditions. Parameters for surface characterization will be

discussed in a later section. Based on the effective permeability of intact and fractured cores through the coreflood setup, the fracture permeability, fracture porosity, and fracture width were calculated according to the equations proposed by Cho et al. (2013):

$$k_{\text{effective}} = k_m + \phi_f k_f \tag{2}$$

$$k_f = 10^3 \frac{w_f^2}{12} \tag{3}$$

$$\phi_f = \frac{4w_f}{10^4 \pi d} \tag{4}$$

$$w_f = \sqrt[3]{30\pi d(k_{\text{effective}} - k_m)} \tag{5}$$

$k_{\text{effective}}$, k_m and k_{f} are the permeability of the fractured cores, permeability of the intact cores (matrix permeability), and the permeability of the tensile fracture; ϕ_f is the tensile fracture porosity; d is the diameter of the intact cores; w_f is the tensile fracture width. The values of fracture permeability, fracture porosity, and fracture width are shown in **Table 4.** Some examples of fracture permeability under different closure stress conditions (Cores #3 to #10) are shown in **Fig. 7.** As shown in Fig. 7, the fracture permeability was extremely high at 300 psi closure stress and then decreased sharply when the closure stress reached up to 1,500 psi. Take Core #3 for example, the fracture permeability was reduced by more than 90% from 108.92 to 9.89 darcies with increased closure stress. Compared to matrix permeability, the fracture permeability was still extremely high. However, the fracture width and fracture porosity shown in Table 4 was

extremely small, especially at high closure stress conditions. The fracture width ranged from 6.86 to 48.74 μm, and the fracture porosity was from 2.45×10^{-4} to 16.29×10^{4}. The tensile fracture is highly conductive but contributes little to the effective permeability of fractured cores due to their limited width and porosity.

Table 4—Properties of tensile fractures at different closure stresses.

	Fracture Permeability, darcy				Fracture Width, μm				Fracture Porosity × 10^4, fraction			
Core #	300 psi	500 psi	1,000 psi	1,500 psi	300 psi	500 psi	1,000 psi	1,500 psi	300 psi	500 psi	1,000 psi	1,500 psi
3	108.92	49.57	23.40	9.89	36.15	24.39	16.76	10.89	12.08	8.15	5.60	3.64
4	123.41	59.92	12.96	9.14	38.48	26.82	12.47	10.47	12.86	8.96	4.17	3.50
5	136.84	44.87	24.92	7.55	40.52	23.21	17.29	9.52	13.54	7.75	5.78	3.18
6	131.11	46.24	25.95	11.30	39.67	23.56	17.65	11.65	13.26	7.87	5.90	3.89
8	108.26	54.52	27.62	17.67	36.04	25.58	18.20	14.56	12.05	8.55	6.08	4.87
9	98.46	45.65	38.17	14.51	34.37	23.40	21.40	13.20	11.49	7.82	7.15	4.41
10	109.75	48.91	30.29	12.47	36.29	24.23	19.07	12.23	12.13	8.10	6.37	4.09
11	84.49	49.89	25.72	13.75	31.84	24.47	17.57	12.84	10.64	8.18	5.87	4.29
12	67.22	47.42	11.48	6.00	28.40	23.85	11.73	8.48	9.49	7.97	3.92	2.83
13	96.42	56.22	27.06	12.64	34.01	25.97	18.02	12.31	11.37	8.68	6.02	4.12
15	99.50	51.75	28.81	8.16	34.55	24.92	18.59	9.90	11.55	8.33	6.21	3.31
17	85.36	48.58	33.65	15.41	32.01	24.15	20.10	13.60	10.70	8.07	6.72	4.54
18	24.57	16.70	8.36	4.49	17.17	14.16	10.02	7.34	5.74	4.73	3.35	2.45
19	50.06	37.04	24.80	20.32	24.51	21.08	17.25	15.61	8.19	7.05	5.77	5.22
20	157.12	62.28	12.47	5.01	43.42	27.34	12.23	7.76	14.51	9.14	4.09	2.59

Table 4. continued

	Fracture Permeability, darcy				Fracture Width, μm				Fracture Porosity × 10^4, fraction			
Core #	300 psi	500 psi	1,000 psi	1,500 psi	300 psi	500 psi	1,000 psi	1,500 psi	300 psi	500 psi	1,000 psi	1,500 psi
21	56.37	48.91	21.07	15.11	26.01	24.23	15.90	13.47	8.69	8.10	5.31	4.50
22	51.43	33.65	12.47	7.12	24.84	20.10	12.23	9.24	8.30	6.72	4.09	3.09
23	21.70	12.64	5.52	3.92	16.14	12.31	8.14	6.86	5.39	4.12	2.72	2.29
26	89.43	71.98	30.29	19.41	32.76	29.39	19.07	15.26	10.95	9.82	6.37	5.10
27	105.2	78.94	19.93	11.48	35.53	30.78	15.46	11.73	11.87	10.29	5.17	3.92
28	56.45	41.28	15.11	10.43	26.03	22.26	13.47	11.19	8.70	7.44	4.50	3.74
29	169.8	125.8	64.31	52.95	45.14	38.85	27.78	25.21	15.08	12.98	9.28	8.42
30	130.9	56.83	19.54	5.52	39.64	26.12	15.31	8.14	13.25	8.73	5.12	2.72
31	111.5	43.58	14.66	4.21	36.58	22.87	13.26	7.11	12.22	7.64	4.43	2.38
32	92.63	42.96	31.94	7.12	33.34	22.71	19.58	9.24	11.14	7.59	6.54	3.09
33	122.8	100.5	47.92	21.70	38.38	34.72	23.98	16.14	12.83	11.60	8.01	5.39
34	82.09	48.75	21.57	13.90	31.39	24.19	16.09	12.92	10.49	8.08	5.38	4.32
35	198.0	175.0	35.32	21.45	48.74	45.82	20.59	16.04	16.29	15.31	6.88	5.36
36	39.46	28.05	20.19	13.12	21.76	18.35	15.56	12.55	7.27	6.13	5.20	4.19
37	162.1	67.08	12.31	5.76	44.11	28.37	12.15	8.31	14.74	9.48	4.06	2.78
38	41.28	24.46	7.55	5.01	22.26	17.13	9.52	7.76	7.44	5.72	3.18	2.59
39	107.7	67.57	34.05	15.84	35.95	28.48	20.21	13.79	12.01	9.52	6.76	4.61
40	75.14	47.67	19.67	12.64	30.03	23.92	15.36	12.31	10.03	7.99	5.13	4.12

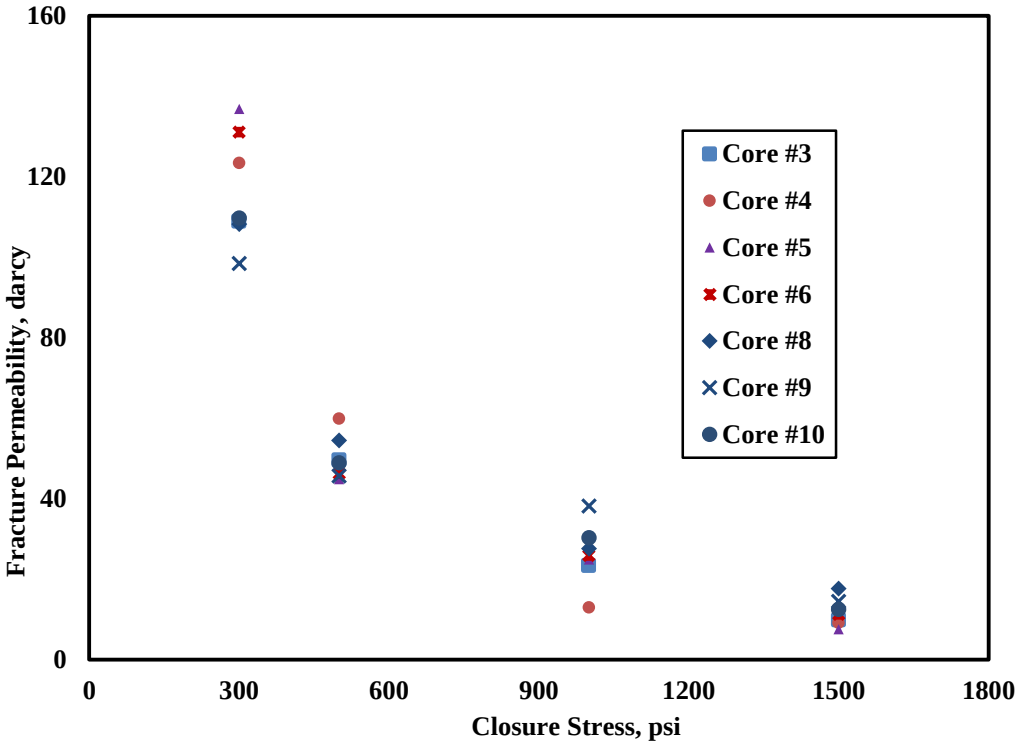

Fig. 7—Permeability of tensile fractures under different closure stress conditions.

4.3 Topography Analysis of Fracture Surfaces

Table 3 shows that the properties of tensile fractures varied greatly especially under low closure stress conditions. For example, the fracture permeability ranged from 21.70 to 197.99 darcies at 300 psi closure stress. Since the faces of tensile fractures were rough with highly varied asperities, it was necessary to conduct surface topography analysis to correlate the surface parameters. Those parameters, well defined by the ISO standards, were used to correlate with the varied fracture permeability to examine the

most important surface textures that contribute substantially to fluid flow across the surface of tensile fractures.

This study used 36 parameters proposed by EN ISO25178-2 (2012), similar to the parameters used by Rodrigues et al. (2011). The parameters included height parameters, spatial parameters, functional parameters (volume), feature parameters, and function parameters (surface). The definitions of various parameters are shown in **Table 5.** After the data files were generated by the surface profilometer, the data files were inputed into a commercial topography analysis software MountainsMap Premium 7.1 (64-bit version). The surface parameters were then calculated automatically, and an output excel sheet containing values for all the parameters was generated together with a 3D contour plot shown in Fig. 5.

Table 5—Parameters of fracture surface topography analysis.

	Parameter		Unit	Comment
Height Parameters	Sq	root mean square height	in.	
	Ssk	height skewness	<no unit>	
	Sku	height krutosis	<no unit>	
	Sp	maximum peak height	in.	
	Sv	maximum pit height	in.	
	Sz	maximum height	in.	
	Sa	arithmetical mean height	in.	
Spatial Parameters	Smr	areal material ratio	%	c = 3.94e-005 in. under the highest peak
	Smc	inverse areal material ratio	in.	p = 10%
	Sxp	peak extreme height	in.	p = 50%- q = 97.5%
	Sal	autocorrelation length	in.	s = 0.2
	Str	texture aspect ratio	<no unit>	s = 0.2
	Std	texture direction	°	Reference angle = 0°
Functional Parameters (Volume)	Vm	material volume	$in.^3/in.^2$	p = 10%
	Vv	dale void volume	$in.^3/in.^2$	p = 10%
	Vmp	peak material volume	$in.^3/in.^2$	p = 10%
	Vmc	core material volume	$in.^3/in.^2$	p = 10%- q = 80%
	Vvc	core void volume	$in.^3/in.^2$	p = 10%- q = 80%
	Vvv	dale void volume	$in.^3/in.^2$	p = 80%
Feature Parameters	Spd	density of peaks	$1/in.^2$	pruning = 5%
		arithmetic mean peak		
	Spc	curvature	1/in.	pruning = 5%
	S10z	ten point height of surface	in.	pruning = 5%

Table 5. continued

	Parameter		Unit	Comment
	S5p	five point peak height	in.	pruning = 5%
	S5v	five point pit height	in.	pruning = 5%
	Sda	mean dale area	in.^{2}	pruning = 5%
	Sha	mean hill area	in.^{2}	pruning = 5%
	Sdv	mean dale volume	in.^{3}	pruning = 5%
	Shv	mean hill volume	in.^{3}	pruning = 5%
Functional Parameters (Surface)	Sk	core height	in.	Gaussian filter- 0.0315 in.
	Spk	reduced peak height	in.	Gaussian filter- 0.0315 in.
	Svk	reduced dale height	in.	Gaussian filter- 0.0315 in.
	Smr1	material ratio for hills	%	Gaussian filter- 0.0315 in.
	Smr2	material ratio for dales	%	Gaussian filter- 0.0315 in.
	Spq	plateau root mean square deviation	<no unit>	Gaussian filter- 0.0315 in.
	Svq	dale root mean square deviation	<no unit>	Gaussian filter- 0.0315 in.
	Smq	material ratio at intersection	<no unit>	Gaussian filter- 0.0315 in.

4.4 Correlations and Predictions of Fracture Permeability

Table 4 shows that the fracture permeability was reduced substantially with increased closure stress. Various correlations of fracture permeability vs. closure stress including exponential, linear, logarithmic, polynomial, power, and moving average were

conducted to determine the best correlation relationships. Exponential correlation of the fracture permeability with closure stress was found to be the most effective one for all 33 cores. All of the correlation data is shown in **Table 6,** and a high R^2 coefficient was achieved.

Table 6—Exponential correlation coefficient of fracture permeability.

Core #	c_1, darcies	c_2, psi^{-1}	R^2 coefficient	Core #	c_1, darcies	c_2, psi^{-1}	R^2 coefficient
3	157.95	0.00188	0.9721	23	27.96	0.00140	0.9423
4	189.29	0.00221	0.9215	26	131.68	0.00133	0.9809
5	198.11	0.00218	0.9433	27	185.80	0.00195	0.9667
6	167.09	0.00184	0.9265	28	82.27	0.00146	0.9607
8	133.92	0.00143	0.9380	29	209.00	0.00099	0.9380
9	125.35	0.00139	0.9055	30	242.38	0.00254	0.9902
10	147.09	0.00165	0.9508	31	201.02	0.00261	0.9850
11	116.10	0.00146	0.9824	32	150.74	0.00192	0.9249
12	123.02	0.00211	0.9745	33	200.14	0.00146	0.9967
13	142.22	0.00164	0.9897	34	110.03	0.00146	0.9626
15	165.86	0.00195	0.9738	35	382.25	0.00203	0.9451
17	112.73	0.00131	0.9619	36	47.48	0.00086	0.9780
18	35.24	0.00140	0.9949	37	295.21	0.00279	0.9607
19	56.80	0.00073	0.9456	38	61.06	0.00179	0.9498
20	292.37	0.00284	0.9715	39	159.77	0.00155	0.9940
21	80.35	0.00117	0.9648	40	104.76	0.00149	0.96480
22	78.23	0.00167	0.9813				

The following equation was proposed for correlation between fracture permeability and closure stress:

$$k_f = c_1 \times e^{-c_2 \times P_c} \tag{6}$$

c_1 is defined as the initial fracture permeability prior to any closure stress in darcies; c_2 is defined as the rate of fracture permeability change with closure stress in psi^{-1}; p_c is the closure stress in psi.

The proposed correlation agreed well with the previous equations proposed for fracture permeability under different confining pressure conditions (Walsh 1981; Raghavan and Chin 2002). The varied values of fracture permeability shown in Table 4 were in accordance with varied values of c_1 in Table 6. Table 6 shows that the initial value of fracture permeability and rate of change varied, depending on the characteristics of each tensile fracture. Some examples were plotted in **Fig. 8** to show their different magnitudes. Some tensile fractures had very high initial fracture permeability (382 darcies) with a high reducing rate (0.00203 psi^{-1}) with closure stress (e.g., Core #35). Some tensile fractures maintained very low initial fracture permeability (less than 40 darcies) and low reducing rates (less than 0.0014 psi^{-1}), e.g., Cores #18 and #23. Cores #20 and #37 had moderate values of fracture permeability and rate of change.

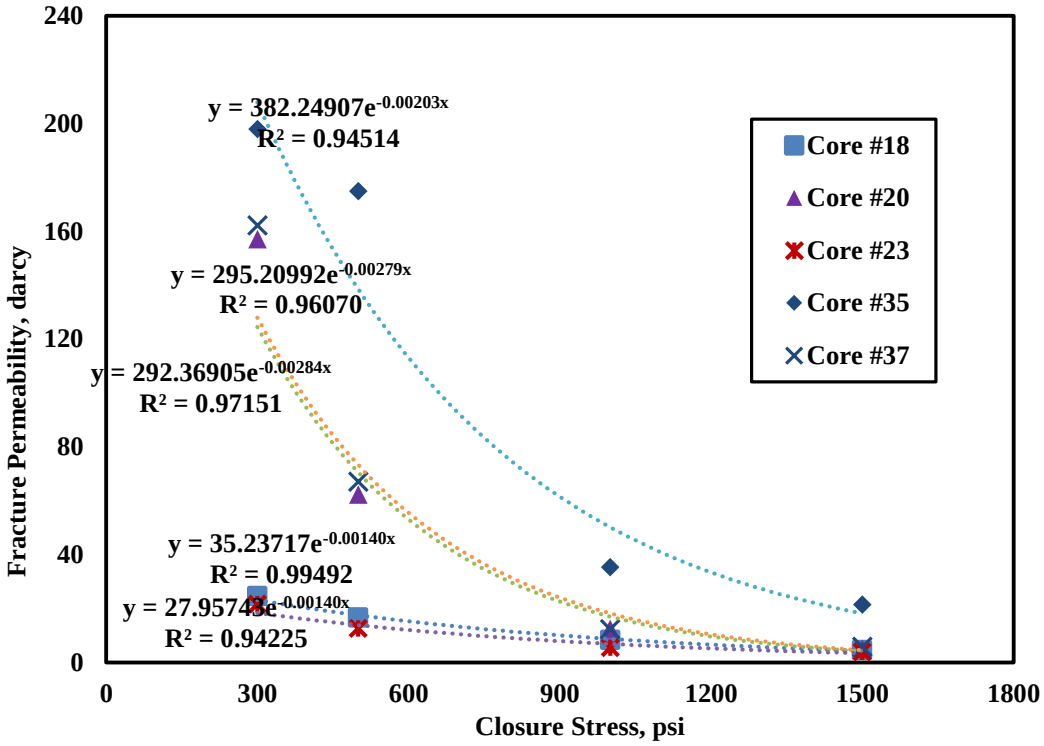

Fig. 8—Exponential permeability correlation of some fractured cores under different closure stress conditions.

The rough face of the tensile fracture shown in Fig. 5 indicate the varied asperities in the fracture surface, which may contribute differently to the dynamics of fluid flow across the fracture plane. Surface parameters from the topographic analysis section accounting for different characteristics of each fracture face were then used to correlate linearly with the parameters in Eq. 5. The purpose was to examine the most important parameters that contribute to fracture permeability. The linear correlation with surface parameters are shown in **Table 7.**

Table 7—Correlation with surface parameters.

	Parameter	Correlation with c_1	Correlation with c_2
Height Parameters	Sq	0.8725	-0.0579
	Ssk	-0.0857	-0.1481
	Sku	0.2260	0.2724
	Sp	0.8705	0.0691
	Sv	-0.7568	0.0490
	Sz	0.5634	0.0617
	Sa	0.7856	-0.1000
Spatial Parameters	Smr	-0.0082	-0.0460
	Smc	-0.2519	-0.0831
	Sxp	0.0047	0.0154
	Sal	0.0997	0.1108
	Str	0.0224	0.0632
	Std	0.0985	0.2017
Functional Parameters (Volume)	Vm	-0.0977	0.1693
	Vv	-0.2472	-0.0800
	Vmp	0.6752	0.1693
	Vmc	0.7827	-0.1551
	Vvc	0.8911	-0.0811
	Vvv	-0.0511	-0.0150
Feature Parameters	Spd	0.0062	-0.0451
	Spc	-0.2105	-0.0098
	S10z	0.7548	-0.0121
	S5p	0.8513	0.0405

Table 7. continued

	Parameter	Correlation with c_1	Correlation with c_2
	S5v	-0.6784	-0.0328
	Sda	0.0473	0.0999
	Sha	-0.0455	-0.0226
	Sdv	-0.1514	-0.0287
	Shv	-0.1721	0.0419
Functional Parameters (Surface)	Sk	-0.1745	0.0224
	Spk	0.0331	-0.0583
	Svk	0.0284	-0.0097
	Smr1	-0.3406	-0.0855
	Smr2	0.2892	0.2190
	Spq	-0.0807	-0.1269
	Svq	0.0328	0.1113
	Smq	0.1580	0.1934

Among all the surface parameters, Sp (maximum peak height), Sa (arithmetical mean height), Vvc (core void volume), Vmc (core material volume), S10z (ten point height of surface), and S5p (five point peak height) were the most related parameters with Vmc having the highest correlation coefficient. The correlation of c_1 with Vmc are shown in **Fig. 9,** and the correlation equation with a correction coefficient of 0.9025 is:

$$c_1 = 6303.6 \times V_{mc} - 138.59 \quad (7)$$

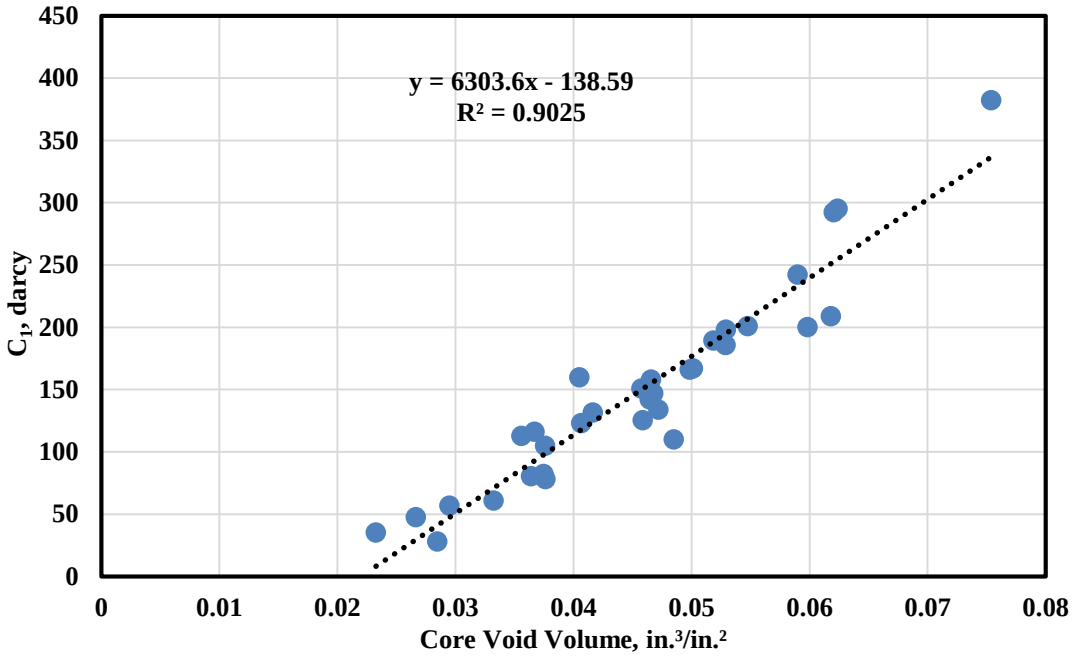

Fig. 9—Linear correlation of core void volume with initial fracture permeability.

However, none of the surface parameters can be correlated with the values of C_2. The parameters C_1 and C_2 are defined as the initial fracture permeability and rate of reduction with closure stress. The correlation results indicated that the initial fracture permeability prior to any closure stress was mostly related to the highest asperities and void volume of the tensile fractures. However, the reducing rate of fracture permeability with closure stress has nothing do with the surface topography. Further studies were conducted to determine the parameters that can correlate well with the values of C_2. The changing rate of fracture permeability with closure stress was more related to the

mechanical properties of tensile fractures. Among all the experimental parameters, rock embedment strength was believed to be the most relevant parameter to rock mechanical properties. Correlation between rock embedment strength and C_2 was conducted, and surprisingly, a relatively high correlation was achieved as shown in **Fig. 10** and Eq. 8:

$$c_2 = -0.001803 \times \ln(RES) + 0.020067 \tag{8}$$

RES is the measured rock embedment strength in psi, and the values were shown in Table 2.

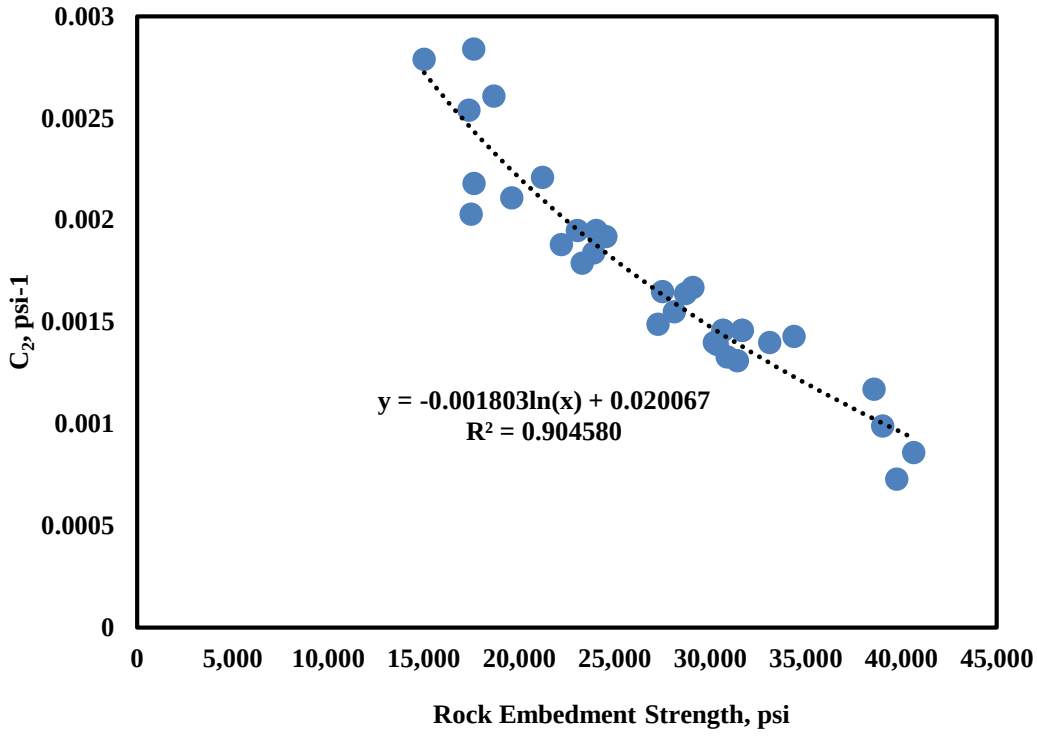

Fig. 10—Logarithmic correlation of C_2 with rock embedment strength.

After desirable correlation parameters were determined, fracture permeability was calculated using Eqs. 6 to 8 and then compared with the actual fracture permeability measurements. The comparison results were shown in **Table 8,** and some examples were shown in **Figs. 11 to 13.** Table 8 showed that the calculated fracture permeabilities are accurate enough to predict actual measured fracture permeability. Among all 33 fractured cores, the predicted fracture permeability seems slightly underestimated under low closure stress with more accurate estimations under high closure stress conditions. This observation is confirmed in Figs. 11 to 13. This may be because the role of surface topography was more important than rock mechanical properties at low closure stress conditions. At low closure stress conditions, more variations in the predicted fracture permeability were observed due to the more pronounced effect of the surface topography. While at high closure stress, the role of rock embedment strength was more obvious than that of surface topography; therefore, the predictions for fracture permeability received more confident values at high closure stress. Overall, the prediction equations for fracture permeability with different closure stresses were:

$$k_f = c_1 \times e^{-c_2 \times P_c} \tag{6}$$

$$c_1 = 6303.6 \times V_{mc} - 138.59 \tag{7}$$

$$c_2 = -0.001803 \times \ln(RES) + 0.020067 \tag{8}$$

Table 8—Predicted fracture permeability under different closure stress conditions.

	Actual Fracture Permeability, darcy				Predicted Fracture Permeability, darcy			
Core #	300 psi	500 psi	1,000 psi	1,500 psi	300 psi	500 psi	1,000 psi	1,500 psi
3	108.92	49.57	23.40	9.89	89.27	59.56	21.66	7.88
4	123.41	59.92	12.96	9.14	104.68	68.72	24.00	8.38
5	136.84	44.87	24.92	7.55	100.70	61.83	18.26	5.39
6	131.11	46.24	25.95	11.30	85.55	58.61	22.77	8.85
8	108.26	54.52	27.62	17.67	83.95	65.59	35.38	19.09
9	98.46	45.65	38.17	14.51	88.20	65.88	31.77	15.32
10	109.75	48.91	30.29	12.47	86.49	62.34	27.49	12.12
11	84.49	49.89	25.72	13.75	76.67	58.15	29.12	14.59
12	67.22	47.42	11.48	6.00	58.64	37.41	12.16	3.95
13	96.42	56.22	27.06	12.64	85.14	62.32	28.57	13.09
15	99.50	51.75	28.81	8.16	87.87	60.34	23.57	9.21
17	85.36	48.58	33.65	15.41	66.76	50.48	25.11	12.49
18	24.57	16.70	8.36	4.49	24.83	19.14	9.98	5.20
19	50.06	37.04	24.80	20.32	41.28	33.98	20.90	12.86
20	157.12	62.28	12.47	5.01	139.13	85.39	25.20	7.44
21	56.37	48.91	21.07	15.11	58.60	47.72	28.56	17.09
22	51.43	33.65	12.47	7.12	50.80	37.36	17.34	8.05
23	21.70	12.64	5.52	3.92	19.42	14.48	6.95	3.34
26	89.43	71.98	30.29	19.41	84.05	63.18	30.95	15.16
27	105.19	78.94	19.93	11.48	92.99	62.88	23.64	8.89

Table 8. continued

Core #	Actual Fracture Permeability, darcy				Predicted Fracture Permeability, darcy			
	300 psi	500 psi	1,000 psi	1,500 psi	300 psi	500 psi	1,000 psi	1,500 psi
28	56.45	41.28	15.11	10.43	51.25	38.87	19.47	9.75
29	169.78	125.78	64.31	52.95	151.91	124.22	75.11	45.42
30	130.96	56.83	19.54	5.52	126.34	77.15	22.48	6.55
31	111.50	43.58	14.66	4.21	94.92	59.49	18.50	5.75
32	92.63	42.96	31.94	7.12	84.93	58.74	23.37	9.30
33	122.78	100.48	47.92	21.70	122.23	91.63	44.59	21.70
34	82.09	48.75	21.57	13.90	65.07	48.78	23.74	11.55
35	197.99	174.96	35.32	21.45	200.50	122.73	35.98	10.55
36	39.46	28.05	20.19	13.12	37.24	30.91	19.39	12.17
37	162.14	67.08	12.31	5.76	132.22	76.64	19.60	5.01
38	41.28	24.46	7.55	5.01	32.68	22.19	8.43	3.20
39	107.71	67.57	34.05	15.84	105.78	76.85	34.58	15.56
40	75.14	47.67	19.67	12.64	59.75	42.93	18.79	8.22

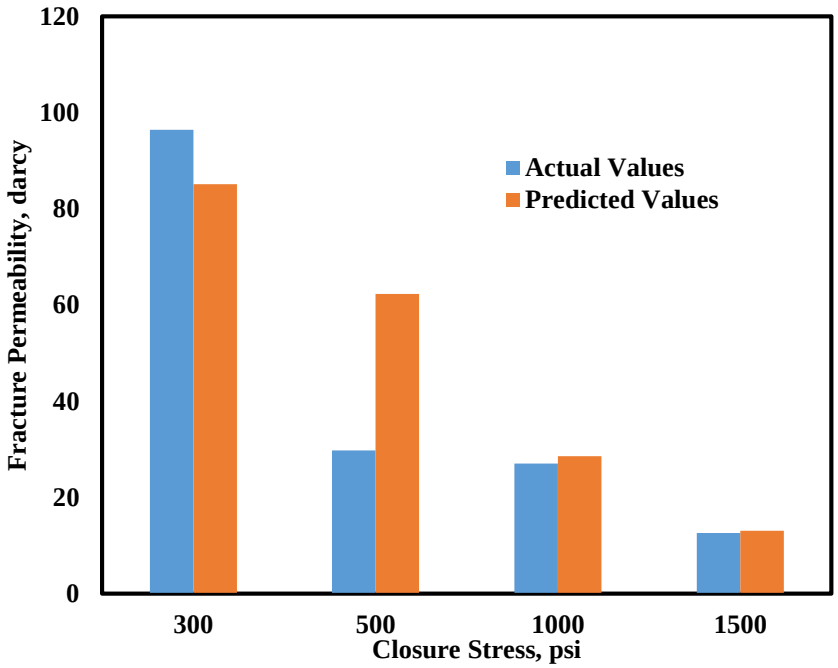

Fig. 11—Actual and predicted values of fracture permeability of Core #13.

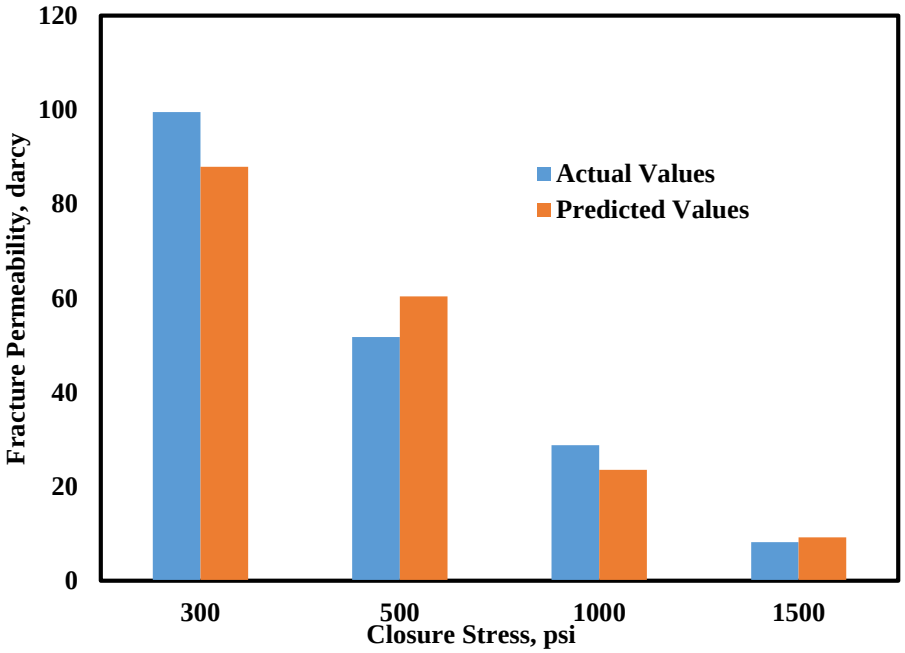

Fig. 12—Actual and predicted values of fracture permeability of Core #15.

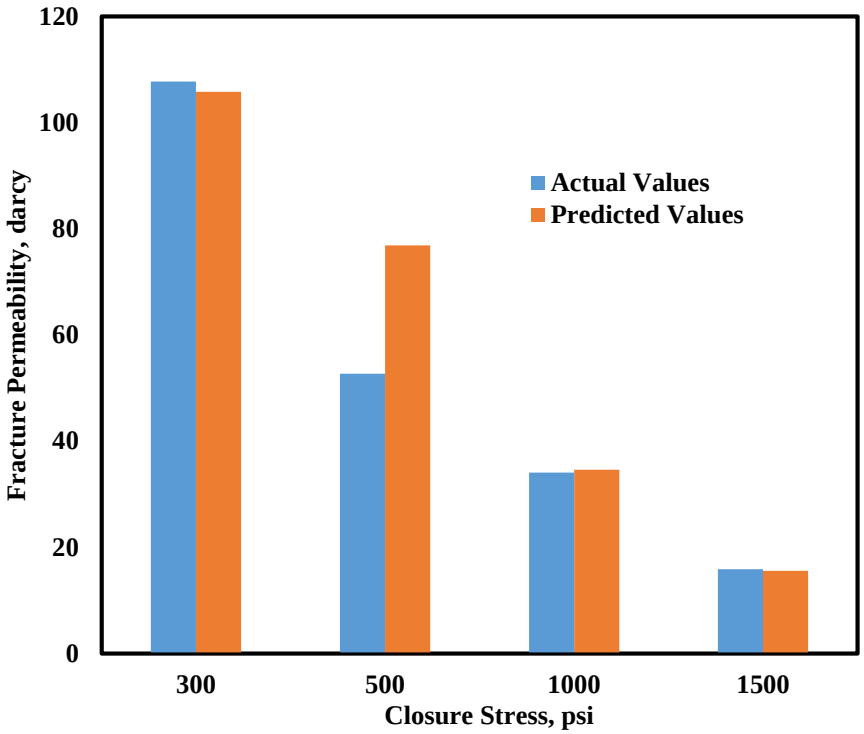

Fig. 13—Actual and predicted values of fracture permeability of Core #39.

5. CFA TESTS WITH 15 WT% HCL

5.1 CFA Tests with 15 wt% HCl at 5 cm^3/min

A CFA test was conducted with a confining pressure of 1,500 psi and a back pressure of 1,000 psi at 250°F. The injection of 15 wt% HCl at 5 cm^3/min continued until wormhole breakthrough across the core occurred. Pressure drop across the core, calcium ions concentration, and acid concentration are shown in **Figs. 14 and 15.**

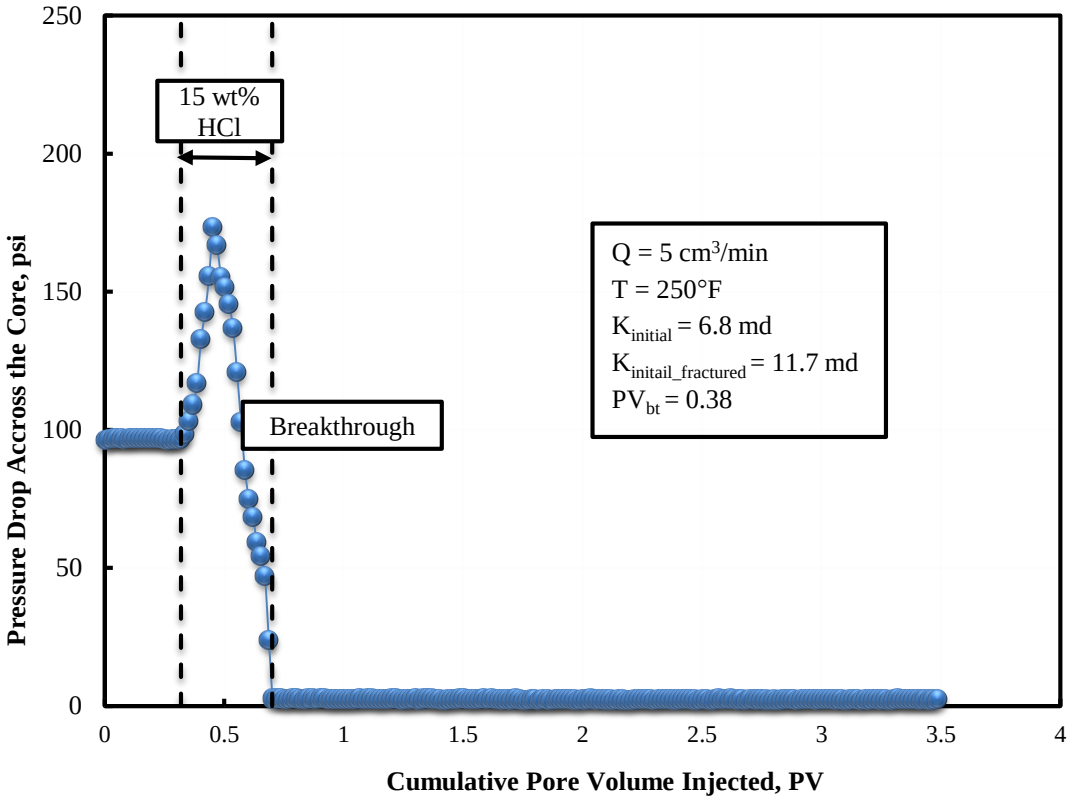

Fig. 14—Pressure drop across the Core #6 with the injection of 15 wt% HCl.

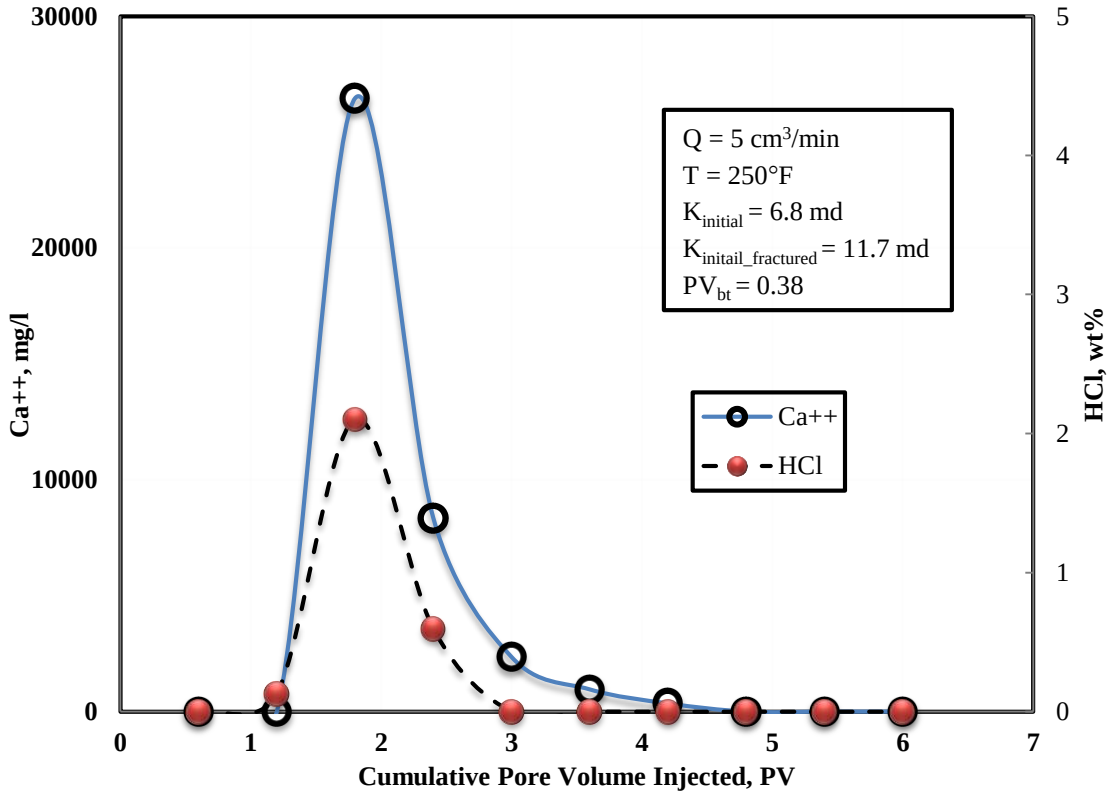

Fig. 15—Calcium concentration and acid concentration in the effluent samples of Core #6.

The initial permeability of fractured core was 11.7 md at 1,500 psi confining pressure. The pore volume at wormhole breakthrough was 0.38, and the maximum calcium concentration was 26,460 mg/l. At 250°F, the reaction rate of 15 wt% with Indiana limestone is fast, and most of the HCl was reacted completely with the maximum value of 2.1 wt% in the effluent samples.

Fig. 16 shows the CT images of Core #6 before and after the CFA test. The wormholes propagate along the fracture plane during the CFA test; as a result, the pore volume of wormhole breakthrough was much less than that of cores without fractures.

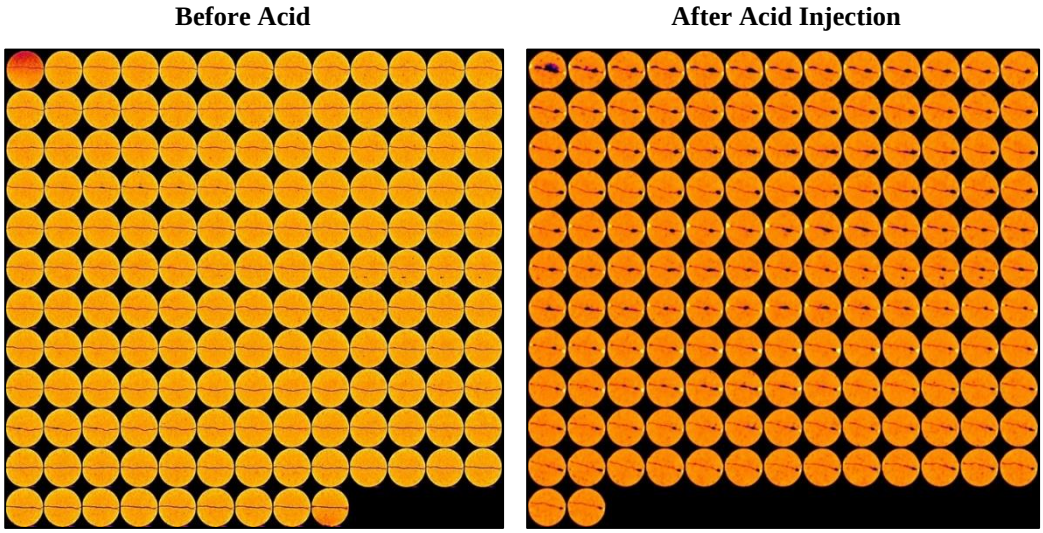

Fig. 16—CT images of Core #6 before and after CFA test.

However, most of the rough surfaces were closed under 1500 psi overburden stress conditions shown in **Fig. 17**. This was also confirmed by 3D profiles of fracture faces of Core #6 after the CFA test shown in **Fig. 18.**

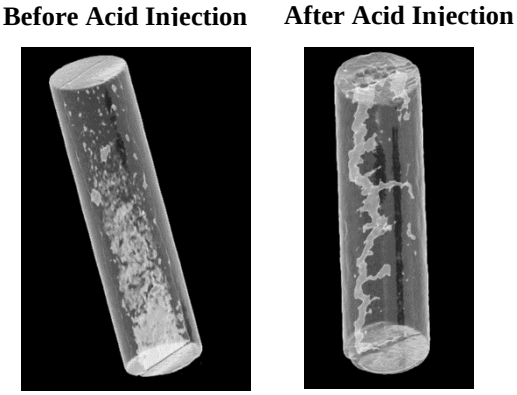

Fig. 17—3D images of Core #6 before and after CFA test.

6A **6B**

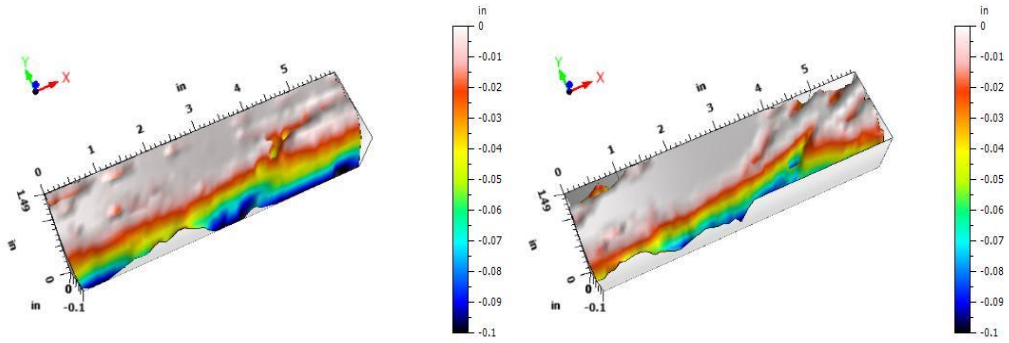

Fig. 18—3D profiles of Core #6 after CFA test.

At 250°F, less pore volume of 15 wt% HCl was required for wormhole breakthrough in the presence of closed fractures, and highly conductive wormholes formed across the core. However, most of the HCl waw spent at 250°F, and a limited fracture length will be developed in the field conditions. Rock embedment strength measurements will be discussed later.

5.2 CFA Tests with Varied Acid Injection Rate

An optimum injection rate has been determined by many investigators in the field of matrix acidizing. The injection rate affects the pore volume of wormhole breakthrough as well as the wormhole structures across the core. It is necessary to determine the effect of injection rate on the propagation characteristics of 15 wt% HCl in the presence of closed fractures. CFA tests at 250°F were conducted at injection rates of 1, 2, 5, 7, and 10 cm^3/min to quantify the effects of injection rate. The properties of

intact cores, fractures cores and tensile fractures are summarized in **Tables 9 to 11**, and the results are shown in **Table 12.**

Table 9—Properties of un-fractured cores.

Core #	Pore Volume, cm^3	Absolute Permeability, md	Compressive Load at Maximum Load, lbf	Compressive Extension at Maximum Load, in.	Young's Modulus, ksi	Rock Embedment Strength, psi
4	24.7	6.6	7,486.6	0.03234	26.3	21,220
5	25.0	5.4	6,172.9	0.05017	23.8	17,622
6	25.0	6.8	5,160.0	0.04197	20.7	23,890
21	20.9	5.6	6,120.8	0.03733	17.7	38,574
39	24.2	10.9	5,964.1	0.05475	17.9	28,110

Table 10—Permeability of fractured cores at different closure stresses.

	Permeability at Different Closure Stress, md				
Core #	300 psi	500 psi	1,000 psi	1,500 psi	Initial Permeability, md
4	165.3	60.3	12.0	9.8	6.6
5	190.7	40.2	19.8	7.8	5.4
6	180.6	43.2	22.1	11.2	6.8
21	54.6	45.2	16.8	12.4	5.6
39	140.3	75.2	33.9	18.2	10.9

Table 11—Properties of tensile fractures at different closure stresses.

Core #	Fracture Permeability, darcy				Fracture Width, μm				Fracture Porosity × 10^4, fraction			
	300 psi	500 psi	1,000 psi	1,500 psi	300 psi	500 psi	1,000 psi	1,500 psi	300 psi	500 psi	1,000 psi	1,500 psi
4	123.4	59.92	12.96	9.14	38.48	26.8	12.47	10.47	12.86	8.96	4.17	3.50
5	136.8	44.87	24.92	7.55	40.52	23.2	17.29	9.52	13.54	7.75	5.78	3.18
6	131.1	46.24	25.95	11.30	39.67	23.6	17.65	11.65	13.26	7.87	5.90	3.89
21	56.37	48.91	21.07	15.11	26.01	24.3	15.90	13.47	8.69	8.10	5.31	4.50
39	107.7	67.57	34.05	15.84	35.95	28.5	20.21	13.79	12.01	9.52	6.76	4.61

Table 12—Maximum calcium concentration and acid concentration with injection of 15 wt% HCl at 250°F.

Core #	Injection Rate, cm^3/min	PVbt	Temp., °F	Maximum Ca++, ppm	Maximum Acid Conc., wt%
4	1	0.87	250	81,380	1.87
5	2	0.49	250	35,020	3.09
6	5	0.38	250	26,460	2.10
21	7	0.23	250	30,580	3.44
39	10	0.3	250	24,920	4.62

The initial permeability of Core #4 was 7.3 md, a little higher than the permeability of intact core. At 1 cm^3/min, the pore volume at wormhole breakthrough was 1.12, and the maximum calcium ion concentration was 81,380 mg/l with a maximum HCl concentration of 1.8 wt%. At 2 cm^3/min, the pore volume at wormhole breakthrough across core #5 was 0.67, the maximum calcium ion concentration was 35,020 mg/l, and the maximum HCl concentration was 3.1 wt%. This confirmed the existence of an optimum injection rate in the presence of closed fractures. At an optimum injection rate, the pore volume at wormhole breakthrough was less, and relatively less acid reacted when acid propagates across the fracture faces. CT scan images at low injection rates of 1 and 2 cm^3/min are shown in **Figs. 19 and 20**.

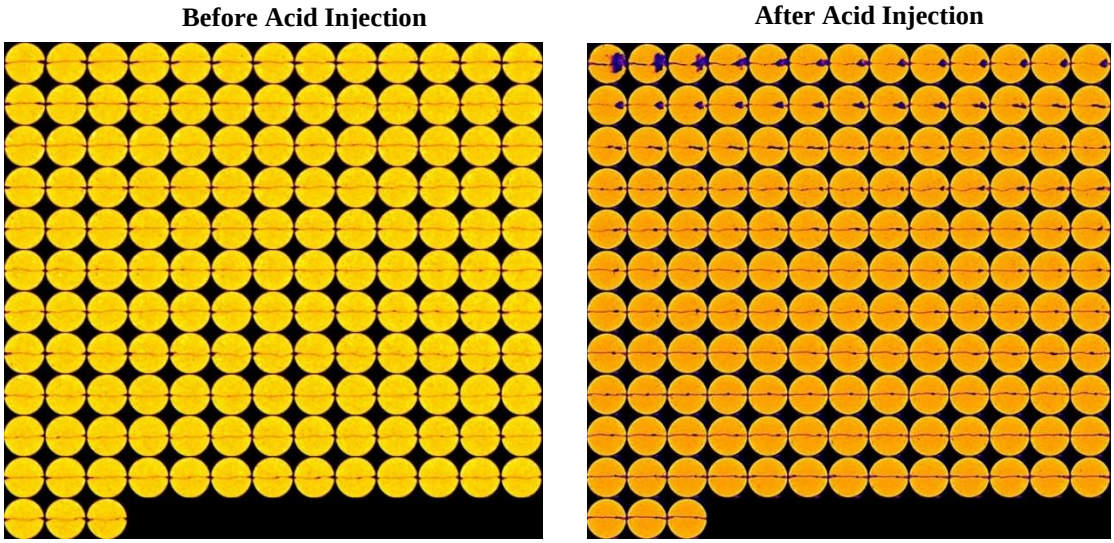

Fig. 19—CT images of Core #4 before and after CFA test.

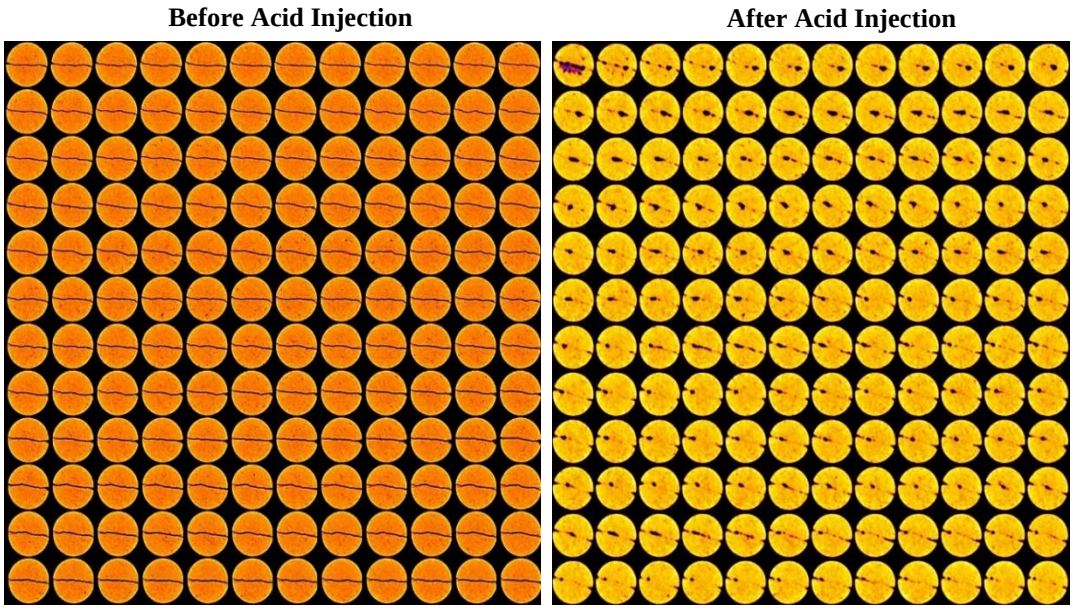

Fig. 20—CT images of Core #5 before and after CFA test.

At 1 cm^3/min, some washout was noted in the inlet section of Core #4 in Fig. 19. Most of the acid reacted in the inlet section, resulting in a smaller wormhole size in the outlet. At 2 cm^3/min, a main and uniform wormhole formed across the core in Fig. 20, and higher acid concentration was determined in the effluent samples. However, most of the acid reacted at all injection rates, and most of the rough surface closed at 1,500 psi of overburden stress during the CFA test. This indicates that although 15 wt% HCl is effective in dissolving calcite in limestone cores and in forming a high conductive wormhole across the fracture faces, the conductive wormhole was short and could hardly penetrate deeply into the formation. In the presence of closed fractures, the optimum injection rate of 15 wt% HCl at 250°F was between 5 and 7 cm^3/min. At an optimum

injection rate, the PVbt was less, and relatively less acid reacted when acid propagates across the fracture faces.

5.3 Acid Etching Profiles and Rock Embedment Strength

For all the CFA tests with the injection of 15 wt% HCl at 250°F, the acid etching profiles are summarized in **Fig. 21,** and the rock embedment strength is shown in **Table 13**. At low and high injection rates (1, 2 and 10 cm^3/min), large part of the fractures were etched by 15 wt% HCl. Well-defined flow channels were developed but with lots of branches. The branches are beneficial to improve the permeability of the fracture plane but too many branches will increase the acid spending rate and limit acid penetration distance. At intermediate injection rates (5 and 7 cm^3/min), flow channels with less branches are developed, indicating the existence of an optimum acid injection rate.

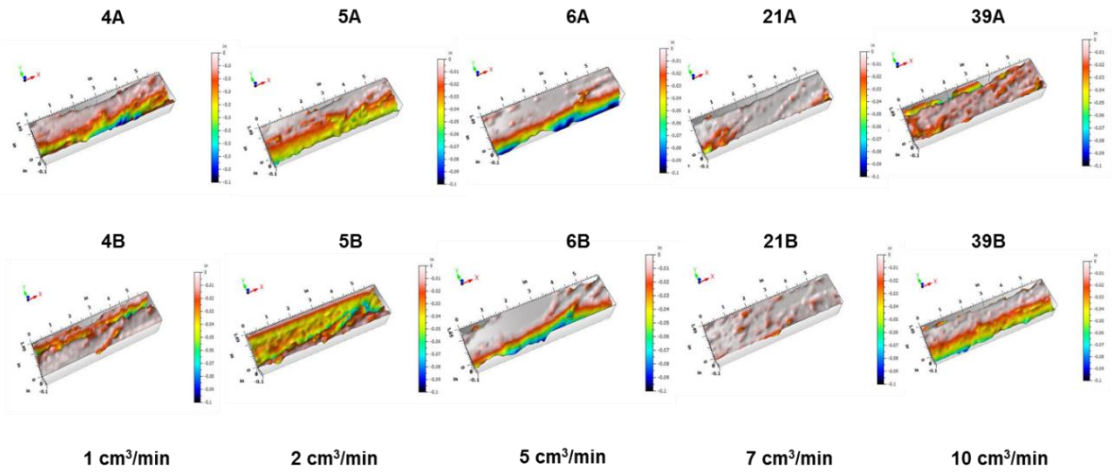

Fig. 21—Acid etching profiles with the injection of 15 wt% HCl at 250°F as a function of injection rate.

The reduction in rock embedment strength is summarized in Table 13. Please note that the value of rock embedment strength before acid injection was taken by averaging all the cores during the tensile fracturing processes. The average value was found to be more suitable to examine the damaging effect on rock mechanical properties by acid injection. Generally, the reduction of rock embedment strength by injection of 15 wt% HCl at 250°F was around 20% on average.

Table 13—Rock embedment strength changes after injection of 15 wt% HCl at 250°F.

Test #	Acid	Label	Temperature	Rock Embedment Strength		
			(°F)	Before (psi)	After (psi)	% change
Core #4	15 wt% HCl	Face A	250	30,486*	20,546	-32.6
1 cm^3/min	15 wt% HCl	Face B	250	30,486*	26,457	-13.2
Core #5	15 wt% HCl	Face A	250	30,486*	24,158	-20.8
2 cm^3/min	15 wt% HCl	Face B	250	30,486*	25,157	-17.5
Core #6	15 wt% HCl	Face A	250	30,486*	23,453	-23.1
5 cm^3/min	15 wt% HCl	Face B	250	30,486*	25,452	-16.5
Core #21	15 wt% HCl	Face A	250	30,486*	25,787	-15.4
7 cm^3/min	15 wt% HCl	Face B	250	30,486*	24,786	-18.7
Core #39	15 wt% HCl	Face A	250	30,486*	25,553	-16.2
10 cm^3/min	15 wt% HCl	Face B	250	30,486*	24,879	-18.4

* Average rock embedment strength for all cores that are fractured.

6. CFA TESTS WITH 20 WT% GLDA

As a replacement for HCl, GLDA has been successfully applied in matrix acidizing carbonate reservoirs. The objective of this section is to examine the effectiveness of GLDA used as a standalone closed fracture acidizing fluid by conducting CFA tests using 20 wt% GLDA at 250°F at various injection rates.

6.1 CFA Tests with 20 wt% GLDA at 1 cm^3/min

CFA test on core #20 at injection rate of 1 cm^3/min was firstly conducted. The initial permeability of the fractured Core #20 was 10.9 md, and the results are shown in **Figs. 22 to 26**.

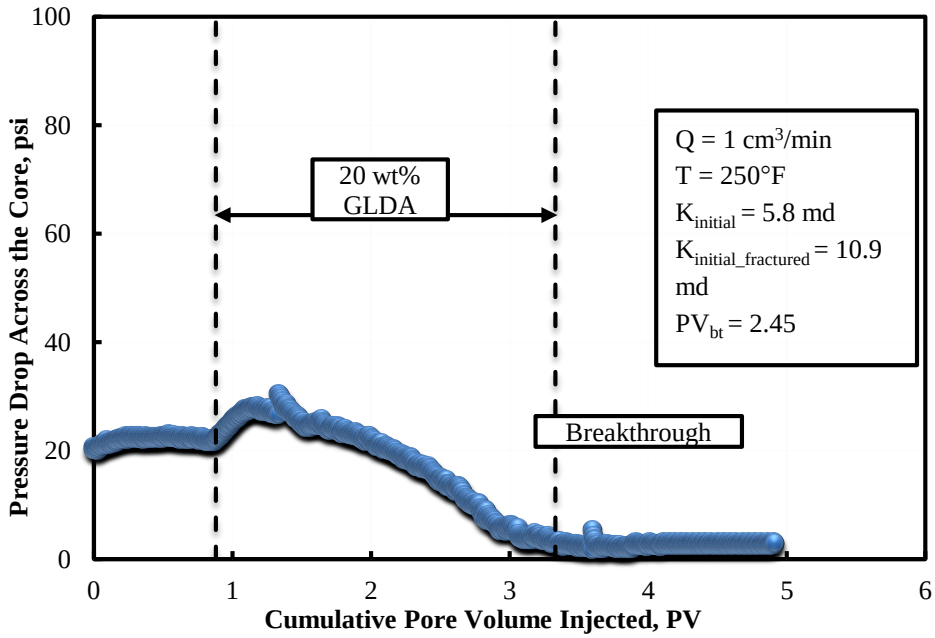

Fig. 22—Pressure drop across the Core #20 with the injection of 20 wt% GLDA.

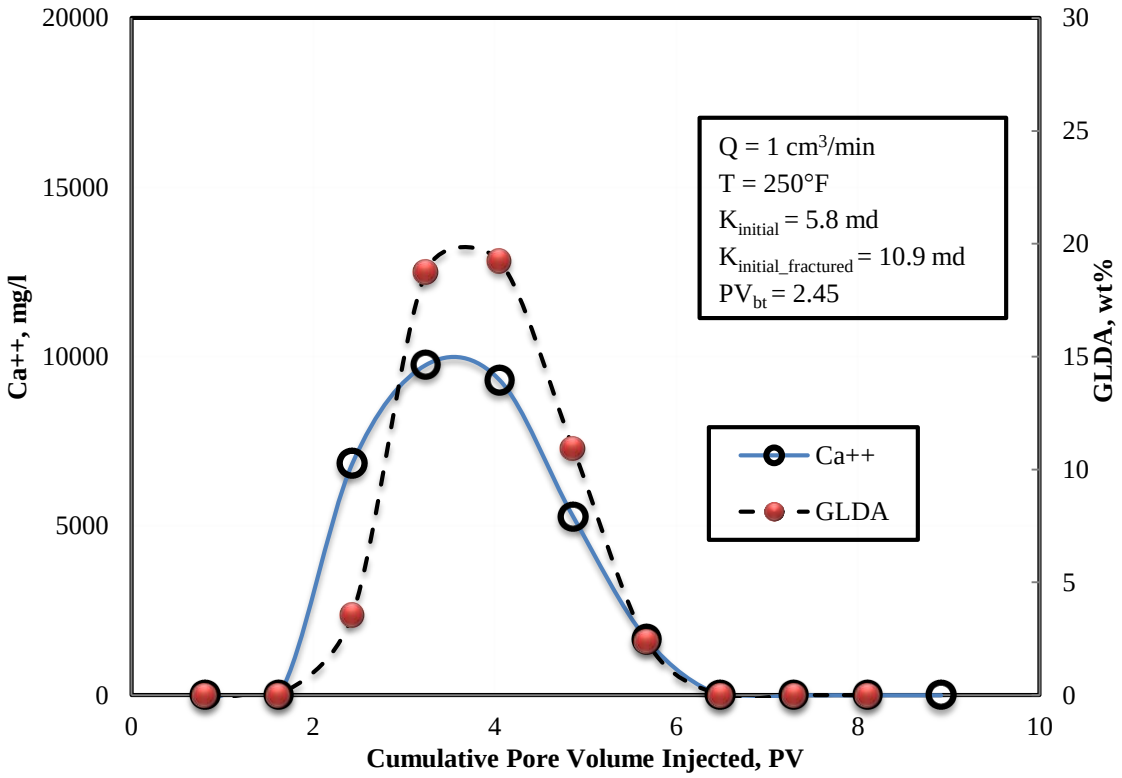

Fig. 23—Calcium concentration and acid concentration in the effluent samples of Core #20.

At 1 cm^3/min, the value of PV_{bt} is 2.45, and the maximum calcium concentration in the effluent samples was found to be 9,754 mg/l. The spent GLDA in the effluent samples were titrated to determine the spent percentage of original injection 20 wt% GLDA together with the concentration of calcium in the effluent samples. After reaching wormhole breakthrough, the fracture surfaces of Core #20 were scanned using the CT scanner and the profilometer to characterize fracture surfaces after acid injection. The results are shown in Figs. 24 to 26.

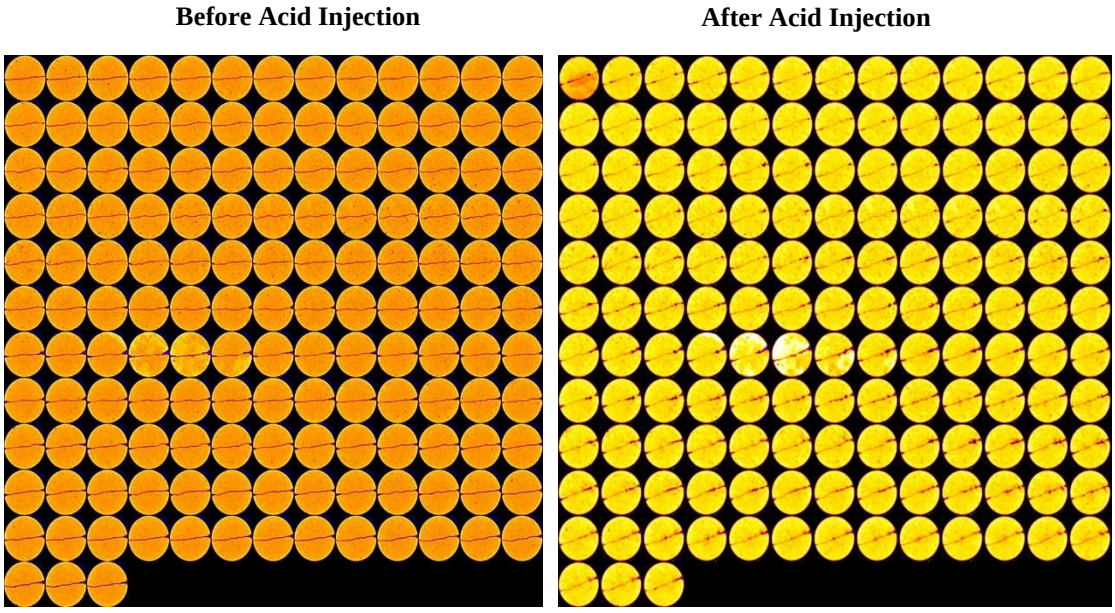

Fig. 24—CT images of Core #20 before and after CFA test.

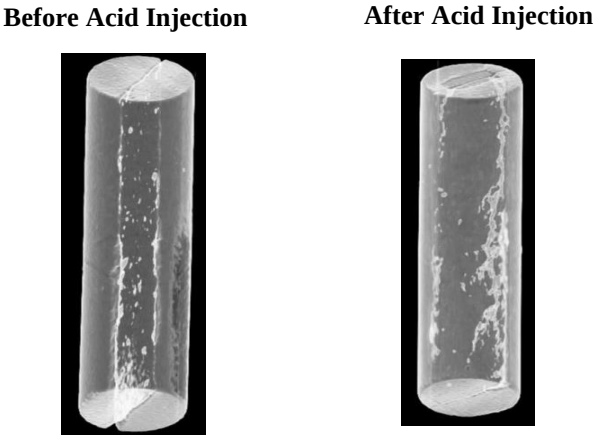

Fig. 25—3D images of Core #20 before and after CFA test.

20A **20B**

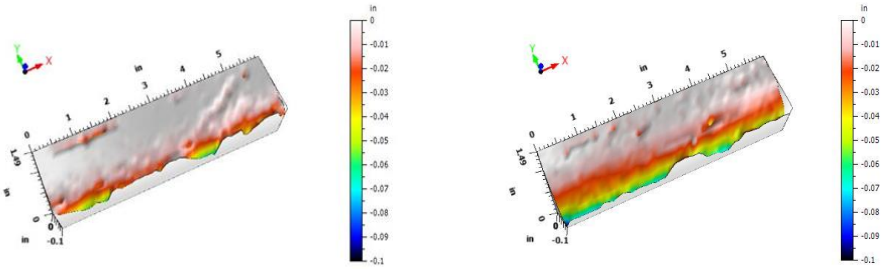

Fig. 26—Acid Etching Profiles after Injection of 20 wt% GLDA at 250°F.

With the injection of 20 wt% GLDA at 1 cm^3/min, flow channels were developed across the fracture plane with little branches. As discussed before, those flow channels will provide high conductive pathways for fluids to flow and sustain high closure stress conditions. Unlike 15 wt% HCl, at a low injection rate, 20 wt% GLDA did not creat facial dissolution.

6.2 CFA Tests with Varied Acid Injection Rate

CFA tests at 250°F were conducted at injection rates of 1, 2, 5, 7, and 10 cm^3/min to quantify the effects of injection rate on the propagation characteristics of 20 wt% GLDA in the presence of closed fractures. The properties of intact cores, fractures cores, and tensile fractures are summarized in **Tables 14 to 16**, and the experimental results are shown in **Table 17.**

Table 14—Properties of un-fractured cores.

Core #	Pore Volume, cm^3	Absolute Permeability, md	Compressive Load at Maximum Load, lbf	Compressive Extension at Maximum Load, in.	Young's Modulus, ksi	Rock Embedment Strength, psi
20	18.5	5.8	6,045.1	0.03208	24.7	17,606
23	25.7	6.5	5,940.6	0.05259	20.8	30,210
38	19.1	6.5	6,193.8	0.05414	19.1	23,287
40	25.9	6.5	6,718.3	0.05030	21.2	27,262
35	24.5	4.9	6,900.6	0.05700	20.3	17,477

Table 15—Permeability of fractured cores at different closure stresses.

	Permeability at Different Closure Stress, md				
Core #	300 psi	500 psi	1,000 psi	1,500 psi	Initial Permeability, md
20	233.8	62.7	10.9	7.1	5.8
23	18.2	11.7	8.0	7.4	6.5
38	37.2	20.5	8.9	7.8	6.5
40	81.9	44.6	16.6	11.7	6.5
35	327.4	272.8	29.2	16.4	4.9

Table 16—Properties of tensile fractures at different closure stresses.

Core #	Fracture Permeability, darcy				Fracture Width, μm				Fracture Porosity × 10^4, fraction			
	300 psi	500 psi	1,000 psi	1,500 psi	300 psi	500 psi	1,000 psi	1,500 psi	300 psi	500 psi	1,000 psi	1,500 psi
20	105.19	78.94	19.93	11.48	35.53	30.78	15.46	11.7	11.87	10.29	5.17	3.92
23	130.96	56.83	19.54	5.52	39.64	26.12	15.31	8.14	13.25	8.73	5.12	2.72
38	41.28	24.46	7.55	5.01	22.26	17.13	9.52	7.76	7.44	5.72	3.18	2.59
40	75.14	47.67	19.67	12.64	30.03	23.92	15.36	12.3	10.03	7.99	5.13	4.12
35	197.99	174.96	35.32	21.45	48.74	45.82	20.59	16.0	16.29	15.31	6.88	5.36

Table 17—Maximum calcium concentration and acid concentration with injection of 20 wt% GLDA at 250°F.

Core #	Injection Rate, cm^3/min	PVbt	Temp., °F	Maximum Ca++, ppm	Maximum Acid Conc., wt%
20	1	2.45	250	9,754	19.2
23	2	2.94	250	21,420	19.5
38	5	4.43	250	13,718	19.5
40	7	4.98	250	20,880	19.3
35	10	5.14	250	15,286	19.7

At 5 cm^3/min, the pore volume at wormhole breakthrough was 4.43, and the maximum calcium concentration of effluent samples was 13,718 mg/l, indicating a slower reaction rate of 20 wt% GLDA compared to that at 1 cm^3/min. For the 20 wt% GLDA, higher injection rate leads to higher PVbt due to the reduction of reaction time between calcium carbonate and acid. More acid needs to be injected to reach wormhole breakthrough at a higher injection rate. The maximum calcium concentration at various injection rates is much smaller than that of 15 wt% HCl, indicating slower reaction rates. No facial dissolution occurred at all injection rates.

6.3 Acid Etching Profiles and Rock Embedment Strength

At 250°F, the acid etching profiles at various injection rates are shown in **Fig. 27,** and the reduction in rock embedment strength is summarized in **Table 18**. At 1 and 2 cm^3/min, well developed flow channels are created across the fracture plane with less branches. At 5 and 7 cm^3/min, less well developed flow channels are created. At high injection rate (10 cm^3/min), too many braches are created along with the main flow channels, which will increase the acid spending rate. At all injection rates, the reduction in rock embedment strength is generally less than 10% for each core shown in Table 18, much less than that of 15 wt%. Much less damaging effect on rock mechanical properties are observed with the injection of 20 wt% GLDA. Therefore, in field conditions, adequate fracture length and fracture face with higher embedment strength will be developed across the closed fracture faces, resulting in substantial acid fracture conductivity.

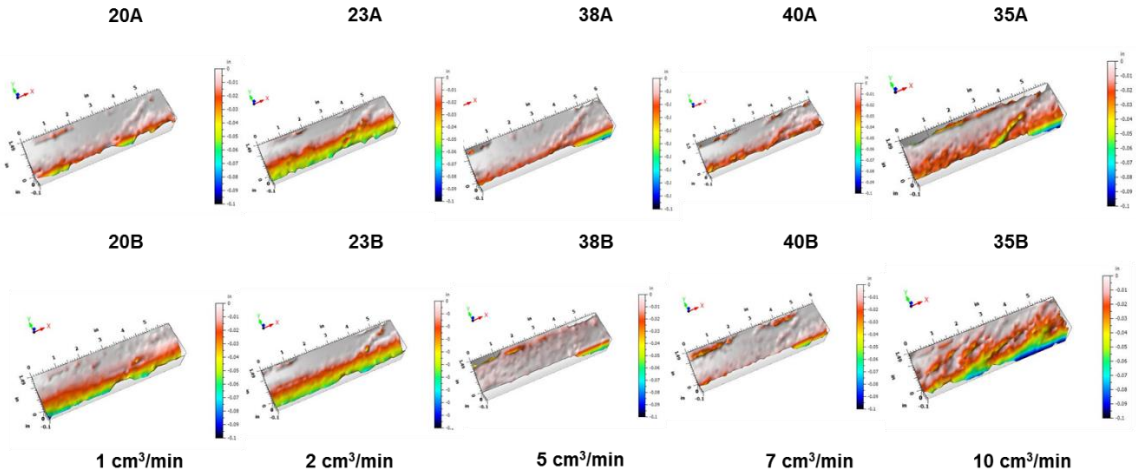

Fig. 27—Acid etching profiles with the injection of 20 wt% GLDA at 250°F as a function of injection rate.

Table 18—Rock embedment strength changes after injection of 20 wt% GLDA at 250°F.

Test #	Acid	Label	Temperature (°F)	Rock Embedment Strength		
				Before (psi)	After (psi)	% change
Core #20 1 cm^3/min	20 wt% GLDA	Face A	250	30,486*	27,757	-9.0
	20 wt% GLDA	Face B	250	30,486*	29,057	-4.7
Core #23 2 cm^3/min	20 wt% GLDA	Face A	250	30,486*	26,645	-12.6
	20 wt% GLDA	Face B	250	30,486*	28,765	-5.6
Core #38 5 cm^3/min	20 wt% GLDA	Face A	250	30,486*	27,789	-8.8
	20 wt% GLDA	Face B	250	30,486*	27,856	-8.6
Core #40 7 cm^3/min	20 wt% GLDA	Face A	250	30,486*	28,456	-6.7
	20 wt% GLDA	Face B	250	30,486*	29,475	-3.3
Core #35 10 cm^3/min	20 wt% GLDA	Face A	250	30,486*	28,412	-6.8
	20 wt% GLDA	Face B	250	30,486*	27,989	-8.2

* Average rock embedment strength for all cores that are fractured.

6.4 CFA Tests at 300°F

CFA tests at 250°F indicated that the injection of 20 wt% GLDA achieved slower acid spending rate and higher rock embedment strength. Since temperature is one of the most important factors that affect well stimulation treatments, the aim of this section is to conduct CFA tests at 300°F to examine the temperature effect on characteristics of acid propagation across the fracture plane. The properties of the cores in the CFA tests are summarized in **Tables 19 to 21,** and the experimental results are shown in **Table 22**. The PVbt, maximum acid concentration, and maximum calcium concentration in the effluent samples are shown in Table 22, and the acid etching profiles at various injection rates are shown in **Fig. 28**.

Table 19—Properties of un-fractured cores.

Core #	Pore Volume, cm^3	Absolute Permeability, md	Compressive Load at Maximum Load, lbf	Compressive Extension at Maximum Load, in.	Young's Modulus, ksi	Rock Embedment Strength, psi
12	23.8	6.4	5,789.0	0.02592	25.2	19,597
11	24.9	8.3	6,787.6	0.03846	14.1	31,661
32	25.6	7.6	4,286.8	0.03833	21.5	24,523
10	25.4	7.2	5,895.9	0.05241	21.0	27,492
8	26.9	9.6	5,169.4	0.03041	22.9	34,377

Table 20—Permeability of fractured cores at different closure stresses.

Core #	Permeability at Different Closure Stress, md				Initial Permeability, md
	300 psi	500 psi	1,000 psi	1,500 psi	
12	70.2	44.2	10.9	8.1	6.4
11	98.2	49.1	23.4	14.2	8.3
32	110.8	40.2	28.5	9.8	7.6
10	140.3	46.8	26.5	12.3	7.2
8	140.0	56.2	26.4	18.2	9.6

Table 21—Properties of tensile fractures at different closure stresses.

Core #	Fracture Permeability, darcy				Fracture Width, μm				Fracture Porosity × 10^4, fraction			
	300 psi	500 psi	1,000 psi	1,500 psi	300 psi	500 psi	1,000 psi	1,500 psi	300 psi	500 psi	1,000 psi	1,500 psi
12	67.22	47.42	11.48	6.00	28.40	23.85	11.73	8.48	9.49	7.97	3.92	2.83
11	84.49	49.89	25.72	13.75	31.84	24.47	17.57	12.84	10.64	8.18	5.87	4.29
32	92.63	42.96	31.94	7.12	33.34	22.71	19.58	9.24	11.14	7.59	6.54	3.09
10	109.75	48.91	30.29	12.47	36.29	24.23	19.07	12.23	12.13	8.10	6.37	4.09
8	108.26	54.52	27.62	17.67	36.04	25.58	18.20	14.56	12.05	8.55	6.08	4.87

Table 22—Maximum calcium concentration and acid concentration with injection of 20 wt% GLDA at 250°F.

Core #	Injection Rate, cm^3/min	PVbt	Temp., °F	Maximum Ca++, ppm	Maximum Acid Conc., wt%
12	1	1.93	300	15,476	19.1
11	2	1.12	300	12,906	19.4
32	5	4.44	300	22,360	19.0
10	7	4.91	300	19,112	19.6
8	10	5.05	300	17,752	19.5

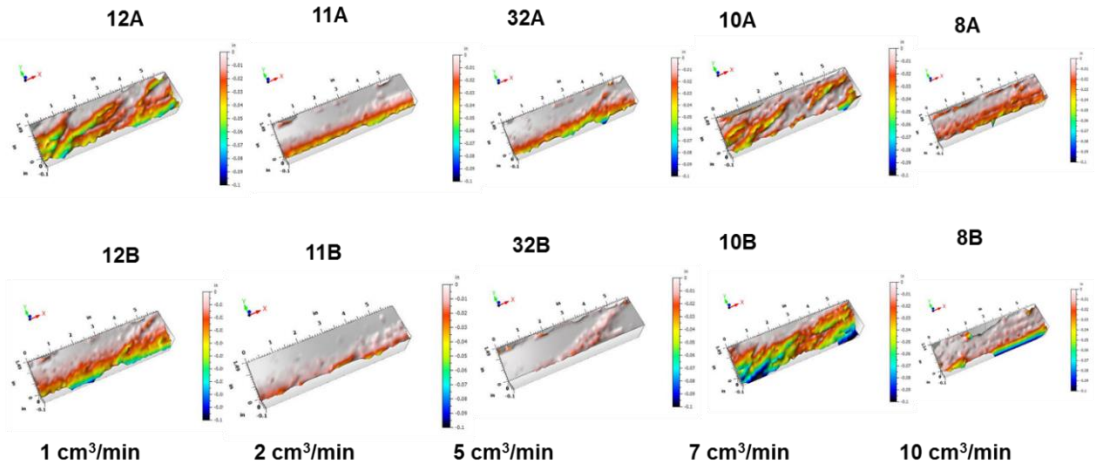

Fig. 28—Acid etching profiles with the injection of 20 wt% GLDA at 250°F as a function of injection rate.

Table 22 shows that the maximum calcium concentration ranges from 12,906 to 22,360 mg/l, quite close to the values at 250°F. The PVbt is close to the values at 250°F as well. High injection rate reduces the reaction time between calcium carbonate and 20 wt% GLDA and thus requires more pore volume for wormhole breakthrough. The acid etching patterns in Fig. 28 indicates more etching at 1, 7, and 10 cm^3/min with more branches. However, less PVbt is required at injection rate of 1 cm^3/min. At 2 cm^3/min, the PVbt is small, and there are dominant channels generated across the fracture plane, which is opposite to the results at 5 cm^3/min.

7. COMPREHENSIVE COMPARISONS OF 15 WT% HCL AND 20 WT% GLDA

Results of previous CFA tests show that 20 wt% GLDA was more effective in creating flow channels across the fracture faces and developing long fracture lengths due to its slow reaction rate characteristics compared to 15 wt% HCl at 250°F. The reduction in rock embedment strength was much less with the injection of 20 wt% GLDA than the 15 wt% HCl. The aim of this chapter is to quantify the difference between 15 wt% HCl and 20 wt% GLDA.

7.1 Etching Patterns and Depths

The 3D acid etching profiles after reaching wormhole breakthrough are shown in Figs 21 and 27, and the quantitative analysis of etching depths is summarized in **Table 23**. Surface profiles of the fractured cores before and after treatments with the injection of 15 wt% HCl or 20 wt% GLDA showed some remarkable differences.

At injection rates of 1 cm^3/min, 2 cm^3/min and 10 cm^3/min, flow channels with lots of branches were developed across the fracture faces in the cores treated with 15 wt% HCl. Table 23 shows that almost 70% of fracture faces were etched by 15 wt% HCl. In successful CFA treatments, well-developed flow channels provide the main fracture conductivity. Branches are beneficial to improvement of fracture permeability but substantial branches will significantly increase acid spending rate and limit acid penetration depth. At the lowest injection rate of 1 cm^3/min, face dissolution was observed, indicative of a too high reaction rate between the rock and the fluid.

Intermediate injection rate of 5 cm^3/min was the optimum case that developed dominant flow channels along the fracture plane. Table 23 shows that 39% of fracture surfaces were affected at 5 cm^3/min.

Table 23—Etching depths of 15 wt% HCl and 20 wt% GLDA after reaching wormhole breakthrough at 250°F as a function of injection rate.

Etching Depth, in.	Percentage of etching depths (%) with 15 wt% HCl at different injection rate (cm^3/min)					Percentage of etching depths (%) with 20 wt% GLDA at different injection rate (cm^3/min)				
	1	2	5	7	10	1	2	5	7	10
0	21	23	61	70	31	50	43	50	51	40
0-0.01	34	9	7	12	25	20	13	28	25	13
001-0.02	21	14	7	7	13	11	8	13	11	15
0.02-0.03	8	14	5	4	10	8	9	4	6	12
0.03-0.04	4	16	5	2	3	5	8	2	3	8
0.04-0.05	3	12	4	2	7	2	8	1	1	4
0.05-0.06	3	6	3	1	4	1	7	1	1	2
0.06-0.07	2	3	2	0	3	1	3	0	1	2
0.07-0.08	2	2	2	0	2	0	1	0	0	1
0.08-0.09	1	1	2	0	1	1	0	0	0	1
0.09-0.10	1	0	1	0	1	0	0	0	0	1
>0.10	1	0	1	0	1	0	0	0	0	1
Total (%)	100	100	100	100	100	100	100	100	100	100

The etching depths of 20 wt% GLDA in Table 23 show that approximately 50% of the fracture surfaces were affected, irrespective of the injection rate. No face dissolution was observed even at the lowest injection rate of 1 cm^3/min. Surface profiles of the cores treated with 20 wt% GLDA showed well-developed flow channels at injection rates of 1 cm^3/min and 2 cm^3/min. Compared to the optimum case of 15 wt% HCl, larger well-developed flow channels with little branches were created by 20 wt% GLDA.

7.2 Acid Spent Rate

Table 24 compares the pore volumes of 20 wt% GLDA and 15 wt% HCl used to reach wormhole breakthrough (PVbt). 15 wt% HCl propagates faster through the length of the core and reacts faster with carbonate, resulting in a lower PVbt. At lower injection rates, the PVbt of HCl increases due to unwanted face dissolution or wash out. GLDA etches a wider part of the fracture surface with much lower reaction rate, resulting in a higher PVbt and a better acid distribution across the entire fracture plane. Increasing the injection rate increases the PVbt as the reaction time between 20 wt% GLDA and carbonate is reduced, and more acids are needed for reaching wormhole breakthrough. **Table 25** lists the percentage of 15 wt% HCl and 20 wt% GLDA reacted with carbonate after reaching wormhole breakthrough. More than 70% of 15 wt% HCl was spent after it propagates across the core. Even at optimum injection case of 5 cm^3/min, 89% of 15 wt% HCl was reacted. Well-developed flow channels were created at this flow rate but with limited acid penetration depth. Compared to 15 wt% HCl, much less of the 20 wt% GLDA was spent after wormhole breakthrough at all injection rates. Surface profiles,

etching depths, and spent percentage all indicate that 20 wt% GLDA forms wider flow channels and penetrate much deeper than 15 wt% HCl. Higher injection rate decreases the spent percentage as reaction time between acid and rock is reduced.

Table 24—Pore volume at breakthrough of 15 wt% Hl and 20 wt% GLDA in closed fractured limestone at 250°F as a function of injection rate.

Injection rate, cm^3/min	15 wt% HCl, PVbt	20 wt% GLDA, PVbt
1	0.87	2.45
2	0.49	2.94
5	0.38	4.43
7	0.23	4.98
10	0.3	5.14

Table 25—Spent percentage of 15 wt% HCl and 20 wt% GLDA after reaching wormhole breakthrough at 250°F as a function of injection rate.

Injection rate, cm^3/min	Spent percentage of 15 wt% HCl, %	Spent percentage of 20 wt% GLDA, %
1	94	38
2	88	44
5	89	35
7	70	30
10	70	27

7.3 Rock Embedment Strength

The change in average rock embedment strength for both fracture faces of all the core samples are summarized in **Table 26.** Results from both faces show a decreasing trend of rock embedment strength after acid injection. 15 wt% HCl weakens the rock significantly more than 20 wt% GLDA, irrespective of the flow rate. At lower flow rates, the decrease in rock strength is more significant for 15 wt% HCl, as the fluid has more time to react with the carbonate rock. The injection rate of GLDA has less influence on the changes in rock embedment strength. A lower rock embedment strength and hence, a weaker rock will increase the risk of fracture closure as the asperities will crush more easily, reducing the conductivity of the fracture.

Table 26—Rock embedment strength changes after treatments with 15 wt% HCl and 20 wt% GLDA at 250°F as a function of injection rate.

Injection rate, cm^3/min	Face	Rock embedment strength change with injection of 15 wt% HCl, %	Rock embedment strength change with injection of 20 wt% GLDA, %
1	A	-32.6	-9.0
	B	-13.2	-4.7
2	A	-20.8	-12.8
	B	-17.5	-5.6
5	A	-23.1	-8.8
	B	-16.5	-8.6
7	A	-15.4	-6.7
	B	-18.7	-3.3
10	A	-16.2	-6.8
	B	-18.4	-8.2

7.4 Fracture Conductivity after Wormhole Breakthrough

Table 27 shows the fracture conductivity of all cores after wormhole breakthrough at 1,500, 2,000, 3,000 and 4,000 psi closure stresses. The increase of closure stress decreased the fracture conductivity as a result of increased contact points and area at high closure stress. The decrease is small because flow channels created in CFA treatments can provide high and stable fracture conductivity under high stress conditions.

Table 27—Fracture conductivity at different closure stress conditions after reaching wormhole breakthrough with 15 wt% HCl and 20 wt% GLDA at 250°F as a function of injection rate.

Acid	Injection rate, cm^3/min	Fracture conductivity in md-ft vs closure stress			
		1500 psi	2000 psi	3000 psi	4000 psi
15 wt% HCl	1	599.69	530.97	492.78	480.90
	2	492.99	441.55	432.22	393.35
	5	480.39	460.75	441.4	431.89
	7	474.22	466.37	433.68	405.50
	10	515.64	491.15	443.59	433.22
20 wt% GLDA	1	533.30	514.55	501.99	492.37
	2	549.15	521.66	491.52	490.25
	5	503.71	495.98	476.83	466.54
	7	537.55	525.77	486.01	476.98
	10	522.54	511.48	501.49	495.01

At the lowest closure stress of 1,500 psi, injection of 15 wt% HCl achieved the highest fracture conductivity at 1 cm^3/min but with up to 118.79 md-ft loss at closure stress of 4,000 psi. At high closure stresses of 3,000 and 4,000 psi, fracture conductivity with injection of 20 wt% GLDA outweighs that of 15 wt% HCl at all injection rates. Besides, irrespective of injection rates, the decrease in fracture conductivity with 20 wt% GLDA (< 60 md-ft) is less than that of 15 wt% HCl (< 120 md-ft). Wider flow channels with little branches achieved with the injection of 20 wt% GLDA contribute to a more stable fracture conductivity.

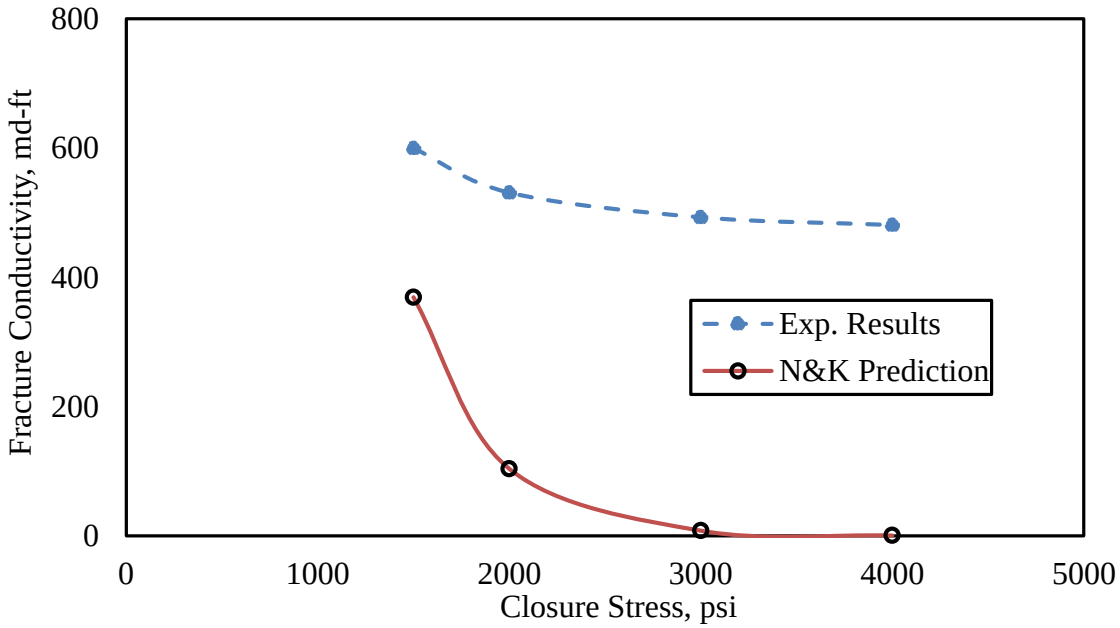

Fig. 29—Fracture conductivity from the CFA test with injection of 15 % HCl at 1 cm^3/min and N&K calculations.

Nierode and Kruk in 1970s proposed correlations to predict the fracture conductivity resulting from traditional acid fracturing treatments. The correlations show that the fracture conductivity is a function of dissolved rock by acid, rock embedment stress and closure stress. According to the predictions, fracture conductivity is substantially decreased by the increment of closure stress since most of the asperities created by acid differential etching are closed under high closure stress conditions. **Fig. 29** shows the fracture conductivity from one of the CFA tests with the injection of 15 wt% HCl at 1 cm^3/min until reaching wormhole breakthrough and the fracture conductivity calculated from Nierode and Kruk. In other words, the fracture conductivity corresponds to the conductivity if we apply traditional acid fracturing treatment with the injection of the same amount of acid. Results show that fracture conductivity by CFA is stable over a wide range of closure stress conditions and cannot be predicted by N&K correlations, especially under high closure stress conditions.

8. DETERMINATION OF LEAKOFF EFFECT

In acid fracturing, the main factor that limits penetration distance of acid and fracture propagation was believed to be excessive leakoff during the acid fracturing process in addition to a fast acid reaction rate. The presence of natural fractures or generated fracture networks by hydraulic fracture treatments deteriorates the problem of leakoff and often leads to the failure of well stimulation treatments.

In this chapter, CFA tests under leakoff conditions were conducted to examine and define the effect of leakoff on acid etching process. The leakoff conditions were simulated by the presence of mini-fractures in the radius direction of the fractured cores and CFA tests were done in a specially designed pressure tapped core holder that can be used to simulate leakoff conditions.

8.1 CFA Test Summary

The cores used for CFA tests in this chapter are Cores #38, #32, #33 and #37. Cores #38 and #32 are the ones without mini-fractures in the radius direction while mini-fractures present in the radius direction of Cores #33 and #37. The CFA tests were conducted at 250 and 300°F, respectively, with the injection of 5 cm^3/min. CT scanning and profilometer characterizations were conducted after CFA tests to examine the leakoff effect. The properties of all the cores are summarized in **Tables 28 to 30,** and the experimental results are presented in **Table 31**.

Table 28—Properties of un-fracture cores.

Core #	Pore Volume, cm^3	Absolute Permeability, md	Compressive Load at Maximum Load, lbf	Compressive Extension at Maximum Load, in.	Young's Modulus, ksi	Rock Embedment Strength, psi
38	19.1	6.5	6,193.8	0.05414	19.1	23,287
32	25.6	7.6	4,286.8	0.03833	21.5	24,523
33	19.1	6.2	5,498.0	0.03009	21.3	30,661
37	22.3	6.6	4,191.7	0.05245	19.3	15,022

Table 29—Permeability of fractures cores at different closure stresses.

Core #	Permeability at Different Closure Stress, md				Initial Permeability, md
	300 psi	500 psi	1,000 psi	1,500 psi	
38	37.2	20.5	8.9	7.8	6.5
32	110.8	40.2	28.5	9.8	7.6
33	163.7	122.8	44.6	17.9	6.2
37	245.6	70.2	11.6	8.2	6.6

Table 30—Properties of tensile fractures at different closure stresses.

Core #	Fracture Permeability, darcy				Fracture Width, μm				Fracture Porosity × 10^4, fraction			
	300 psi	500 psi	1,000 psi	1,500 psi	300 psi	500 psi	1,000 psi	1,500 psi	300 psi	500 psi	1,000 psi	1,500 psi
38	41.28	245	7.55	5.01	22.26	17.13	9.52	7.76	7.44	5.72	3.18	2.59
32	92.63	43	31.94	7.12	33.34	22.71	19.58	9.24	11.14	7.59	6.54	3.09
33	122.78	100	47.92	21.70	38.38	34.72	23.98	16.14	12.83	11.60	8.01	5.39
37	162.14	67.1	12.31	5.76	44.11	28.37	12.15	8.31	14.74	9.48	4.06	2.78

Table 31—PVbt, maximum calcium concentration and maximum acid concentration.

Core #	Injection Rate, cm^3/min	PVbt	Temp., °F	Maximum Ca++, ppm	Maximum Acid Conc., wt%
38	5	4.43	250	13,718	19.5
32	5	4.44	300	22,360	19.0
*33	5	7.64	250	23,400	19.6
*37	5	5.56	300	17,898	19.7

*Leakoff from the main fracture plane.

Table 31 shows that the presence of mini-fractures increased the PVbt substantially. Though, under leakoff conditions, the leakoff in the radius direction decreased the flow rate in the main fracture plane and thus increased the reaction time between calcium carbonate and 20 wt% GLDA. Previous CFA tests showed that less PVbt is required at low injection rate. However, the leakoff of live acid into radius direction outweighs this effect and increased the pore volume for reaching wormhole breakthrough. The concentrations of calcium in the effluent samples are quite similar to that of CFA tests without mini-fractures in the radius direction.

8.2 CT Scan Images

The CT scan images before and after CFA tests for all the cores are shown in **Figs. 29 to 34**. Red arrows in Figs. 29 and 30 show the presence of mini-fractures in the radius direction. The CT images in Figs. 31 and 32 are the cores that were closed fracture acidized without mini-fractures in the radius direction. Compared to the ones that are closed fracture acidized shown in Figs. 33 and 34, there are less etching in the fracture plane. In the areas that are closer to the mini-fractures in the radius direction, there were more etching occurring in the fracture plane. More etching can be beneficial to the fracture conductivity. However, more etching in the fracture plane will also increase the acid spending rate, reducing the penetration of live acid.

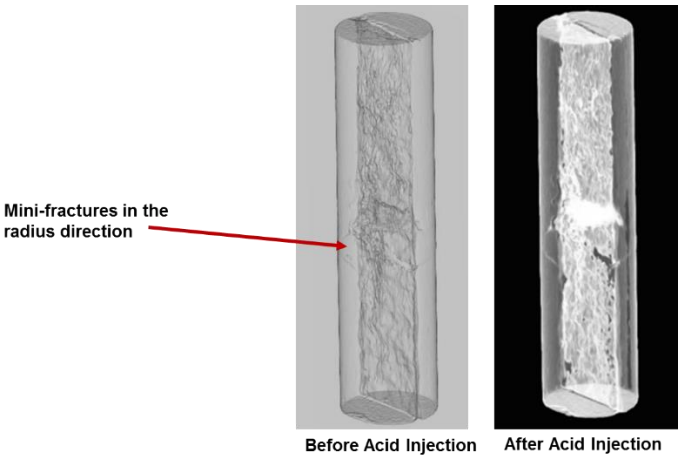

Fig. 30—3D CT images of Core #33.

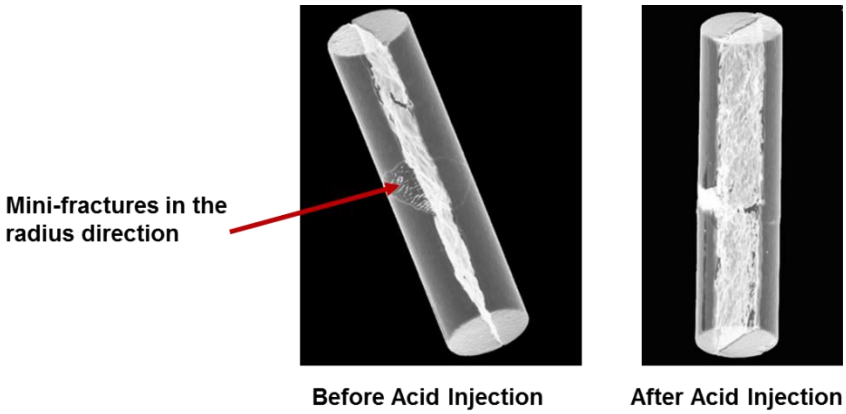

Fig. 31—3D CT images of Core #37.

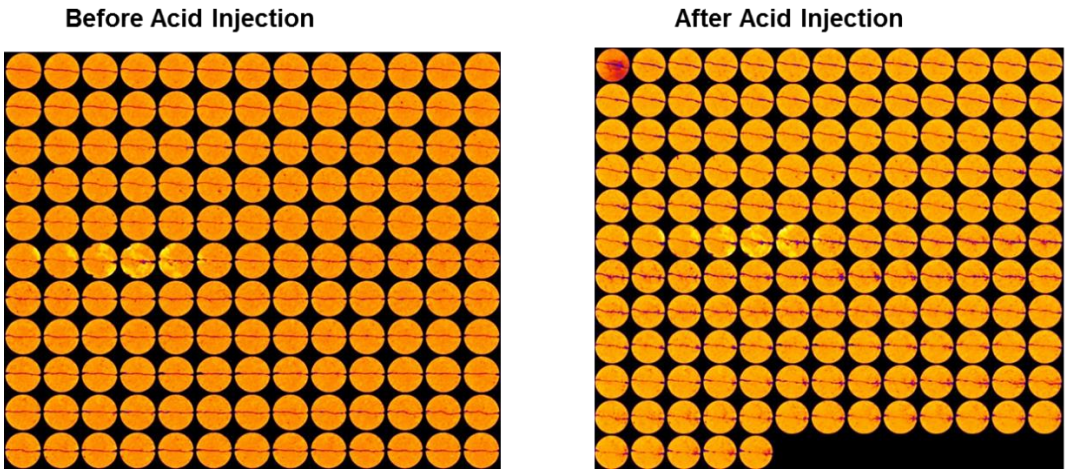

Fig. 32—CT images of Core #38 (without mini-fractures).

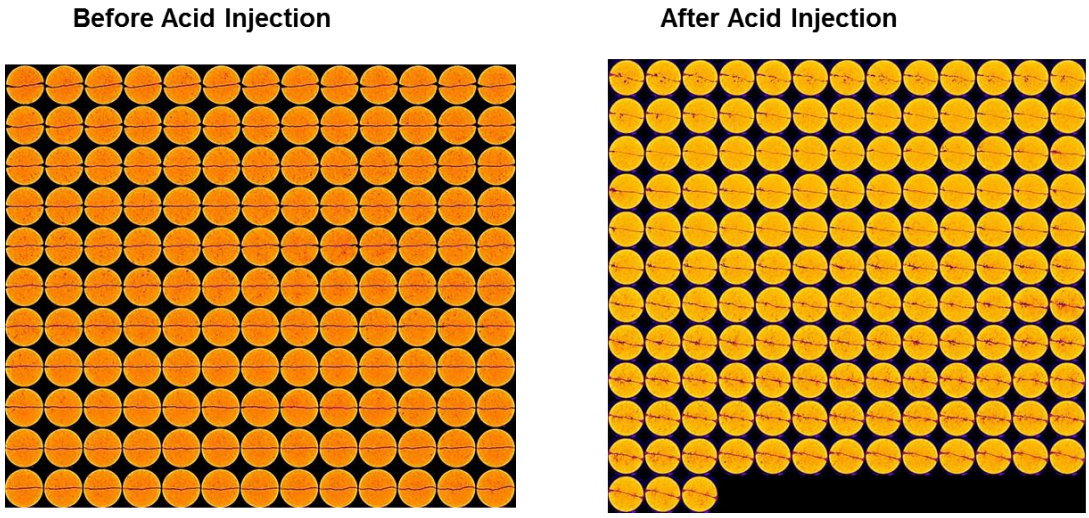

Fig. 33—CT images of Core #32 (without mini-fractures).

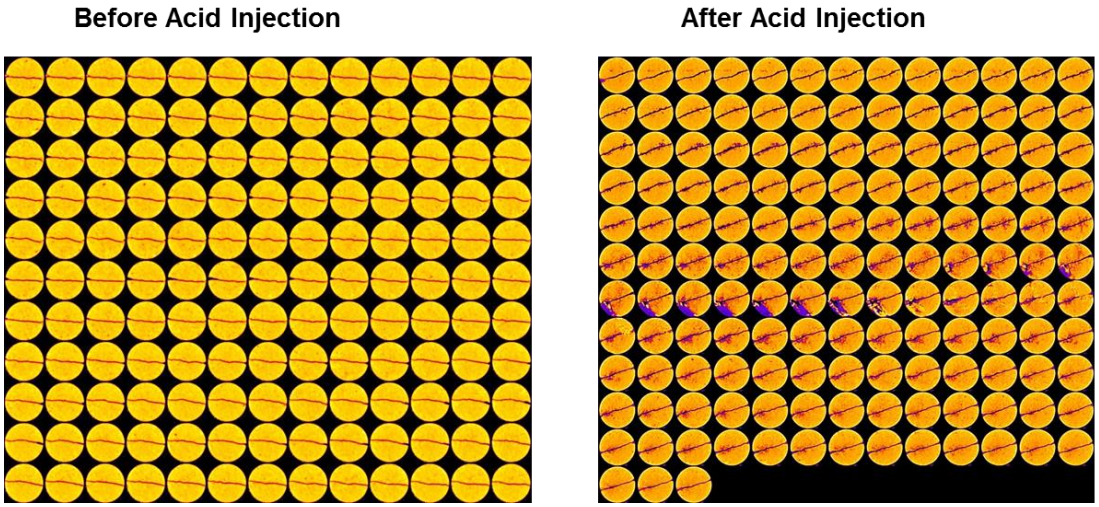

Fig. 34—CT images of Core #33 (without mini-fractures).

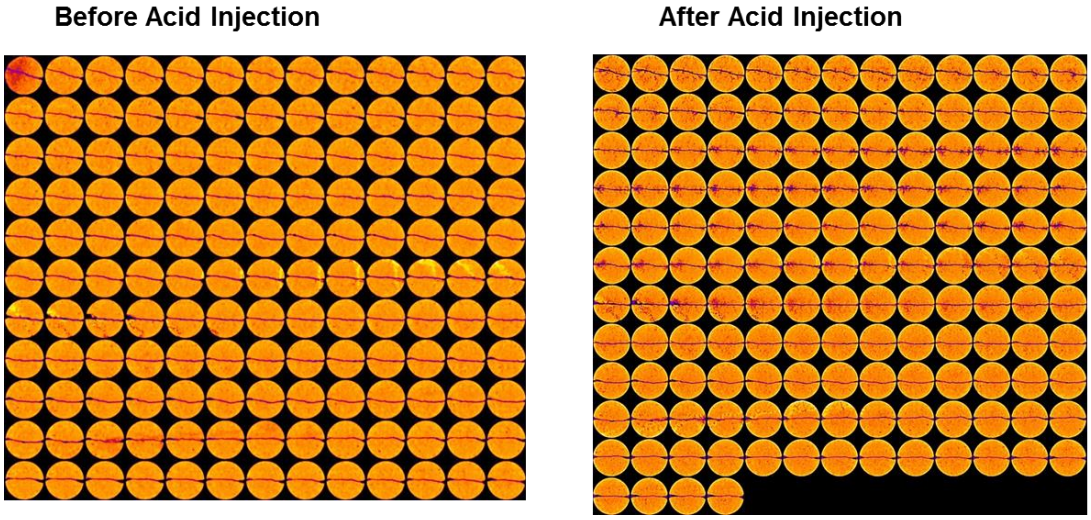

Fig. 35—CT images of Core #37 (without mini-fractures).

8.3 Acid Etching Profiles

The percentage of acid spending and fracture face etching in the presence of mini-fractures in radius direction are summarized in **Table 32,** and the acid etching profiles are shown in **Figs. 35 and 36.**

Results show that more etching and more acid spending occurred if leakoff conditions exist. At 250°F, the PVbt was increased from 4.43 to 7.64. The value of PVbt increased from 4.44 to 5.56 at 300°F. The higher increment at 250°F was due to more etching occurred, shown in previous CT scan images. Besides, the ratio of leakoff rate to the total injection rate in the CFA test conducted at 250°F is 37%, more than the CFA test at 300°F with a ratio value of 24%. Generally, the leakoff rate is moderate in those two CFA tests.

Table 32—Acid spent percentage and percentage of fracture face etching in the presence of mini-fractures.

Injection Rate, cm^3/min	Leakoff percentage, %	PVbt	Temp., °F	Spent percentage, wt%	Fracture face etching, %
5	0	4.43	250	35	50
5	0	4.44	300	46	46
*5	37	7.64	250	45	55
*5	24	5.56	300	51	53

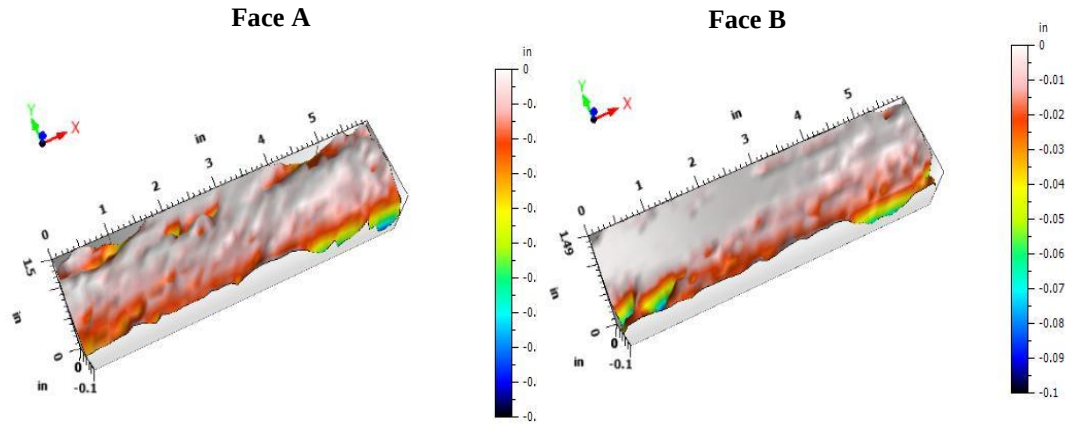

Fig. 36—Acid etching profiles of Core #33.

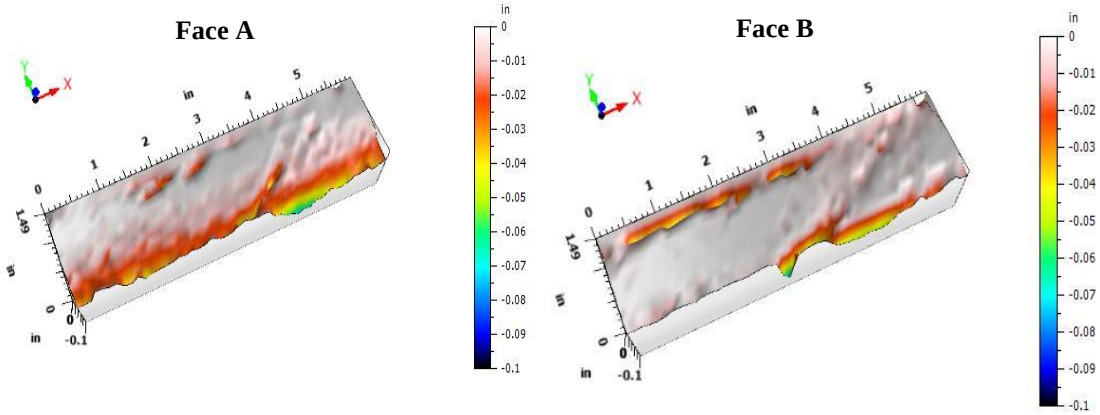

Fig. 37—Acid etching profiles of Core #37.

9. DISCUSSIONS ON FRACTURE CONDUCTIVITY

Previous CFA tests were stopped after reaching wormhole breakthrough across the fracture plane. High conductive wormholes or flow channels are created in the fracture plane; however, the fracture conductivity shown in Table 27 was not high enough due to relatively small etched widths compared to traditional acid fracturing treatments. The aim of this section is to examine the acid etching behaviors and fracture conductivity after continued acid injection for some time after reaching wormhole breakthrough.

9.1 CFA Test Summary

The CFA tests were done on the cores that achieved well developed flow channels across the fracture plane with small value of PVbt for both 15 wt% HCl and 20 wt% GLDA. The cores selected are Cores #20, #23, #21, and #39 for the CFA tests. The etching time after PVbt for 15 wt% HCl was specified at 5 minutes and 30 minutes for 20 wt% GLDA.

Table 33 shows the experimental results for those four cores. After etching for 5 more minutes at PVbt, the percentage of acid spent was 43 wt% and 41 wt%, respectively, for Cores #21 and #39. The spent percentage is less than the cores after reaching wormhole breakthrough due to high flow capacity of created wormholes. However, the acid spent percentage is still high, limiting the penetration distance of live acid. For 20 wt% GLDA, the acid spent percentage has decreased substantially to 16

wt% and 11 wt%, respectively. Therefore, deep penetration can be achieved with the injection of 20 wt% GLDA.

Table 33—CFA tests with continued acid injection after wormhole breakthrough.

Core #	Acid	Injection rate, cm^3/min	Injection time after wormhole breakthrough, minutes	Spent percentage, wt%
39	15 wt% HCl	7	5	43
21		10	5	41
20	20 wt% GLDA	7	30	16
23		2	30	11

9.2 CT Scan Images

The CT scan images for those 4 cores after reaching wormhole breakthrough and continued acid injection after PVbt are shown in **Figs. 37 to 40**. Results show that the sizes of wormholes or flow channels are enlarged after continued acid injection after PVbt for both 15 wt% HCl and 20 wt% GLDA. Those enlarged wormholes or flow channels can provide excellent fracture conductivity for fluids to flow. For CFA tests, the acid can be firstly injected at optimum flow rate to create dominate flow channels across fracture plane and then continuously injected to enlarge the width and create more etching areas.

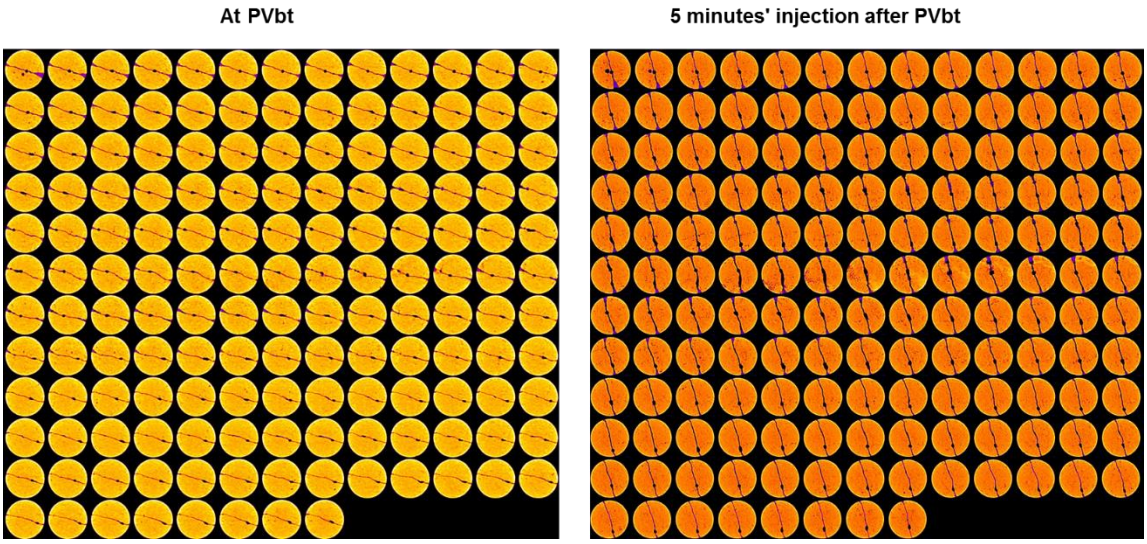

Fig. 38—CT scan images of Core 21 with the injection of 15 wt% HCl at 250°F.

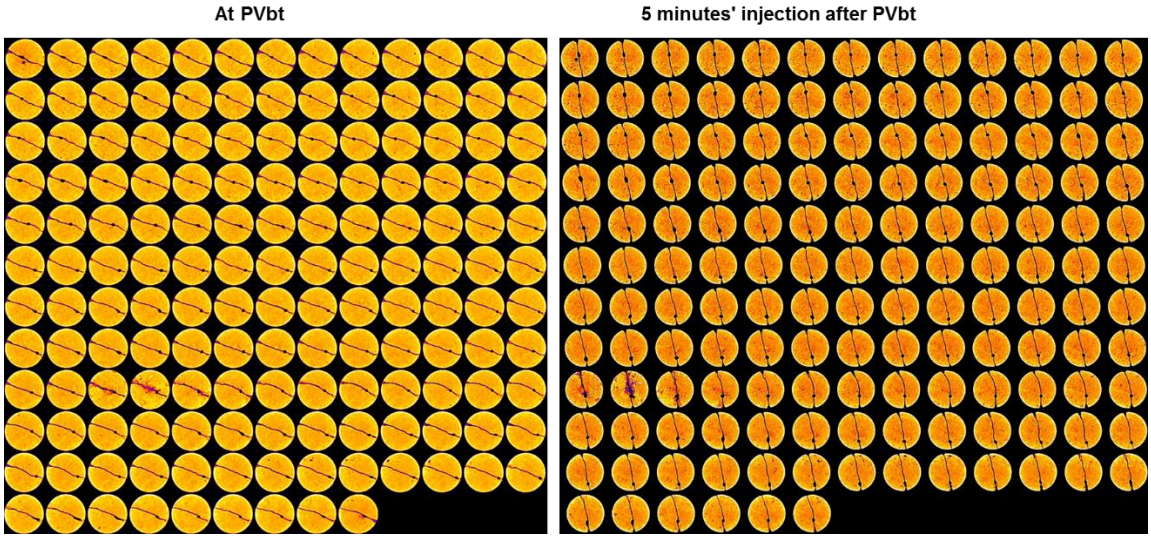

Fig. 39—CT scan images of Core 39 with the injection of 15 wt% HCl at 250°F.

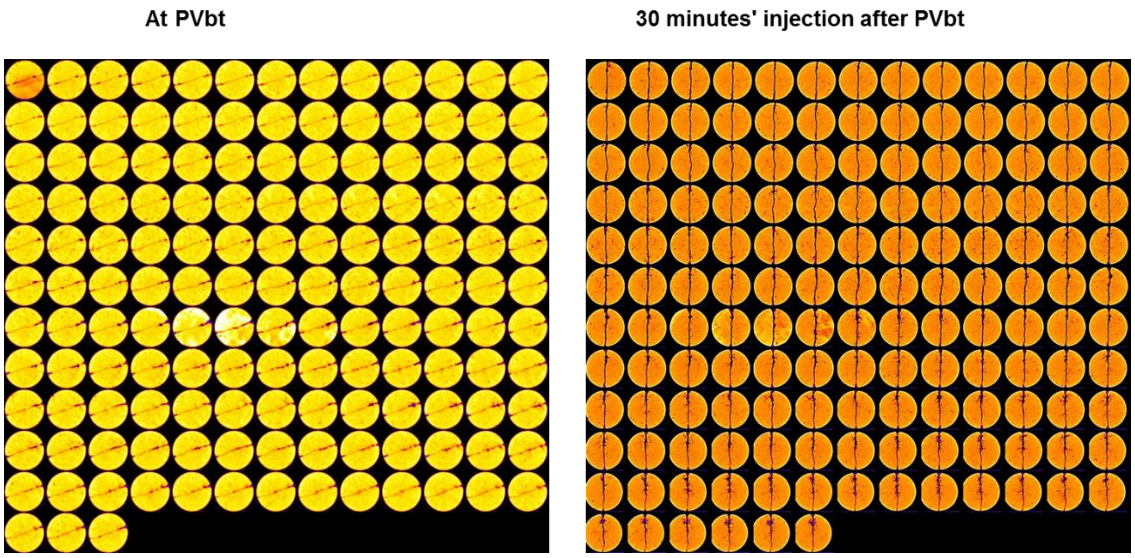

Fig. 40—CT scan images of Core 20 with the injection of 20 wt% GLDA at 250°F.

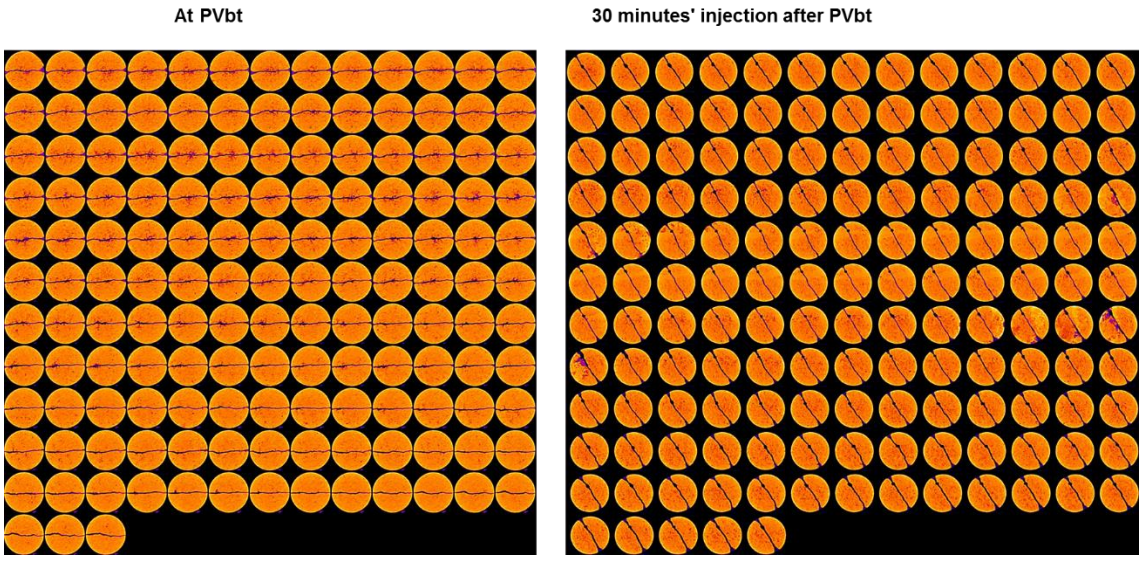

Fig. 41—CT scan images of Core 23 with the injection of 20 wt% GLDA at 250°F.

9.3 Acid Etching Profiles

The surface profiles after acid injection and acid etching profiles for all the cores are shown in **Figs. 41 to 48**. The injection time after PVbt with the injection of 15 wt% HCl is 5 minutes, and the injection time of 20 wt% GLDA is 30 minutes after PVbt. Note that the color scale bar for acid etching depths are different for the one right after wormhole breakthrough and the one with continued acid injection after PVbt.

Take Core #21 for example, the etching depths were substantially increased and the etching areas were extended to the whole fracture plane shown in Fig. 42. Rough surface was created by varied acid etching depths. Fig. 41 shows that actual fracture surface topography of Core #21 after continued 15 wt% HCl injection for 5 more minutes. Pillars shown by white and red areas in Fig. 41 provide support to sustain the high closure stress while the green and yellow areas with greater etching depths provide the conductive flow pathways for fluid to flow. The same phenomenon was observed for the cores treated with 20 wt% GLDA.

The injection rates for cores treated with 15 wt% HCl were 7 and 10 cm^3/min while the injection rates of 20 wt% GLDA were 2 and 7 cm^3/min, respectively. Figs 42 and 44 show that rough etching patterns were formed across the fracture plane at high injection rates. For the cores injected with 20 wt% GLDA, Fig. 46 shows a differential channel behaviors at 7 cm^3/min while Fig. 48 indicates a much rougher surface at 2 cm^3/min. Therefore, injection rate matters to the actual acid etching patterns, and acid flow tests should be conducted to determine the optimum treatment parameters.

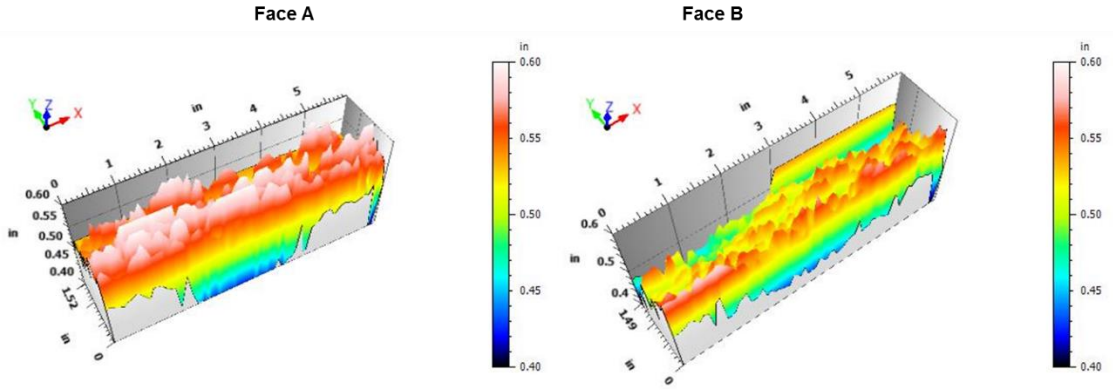

Fig. 42—Surface profiles of Core #21 with injection of 15 wt% HCl for 5 minutes after PVbt.

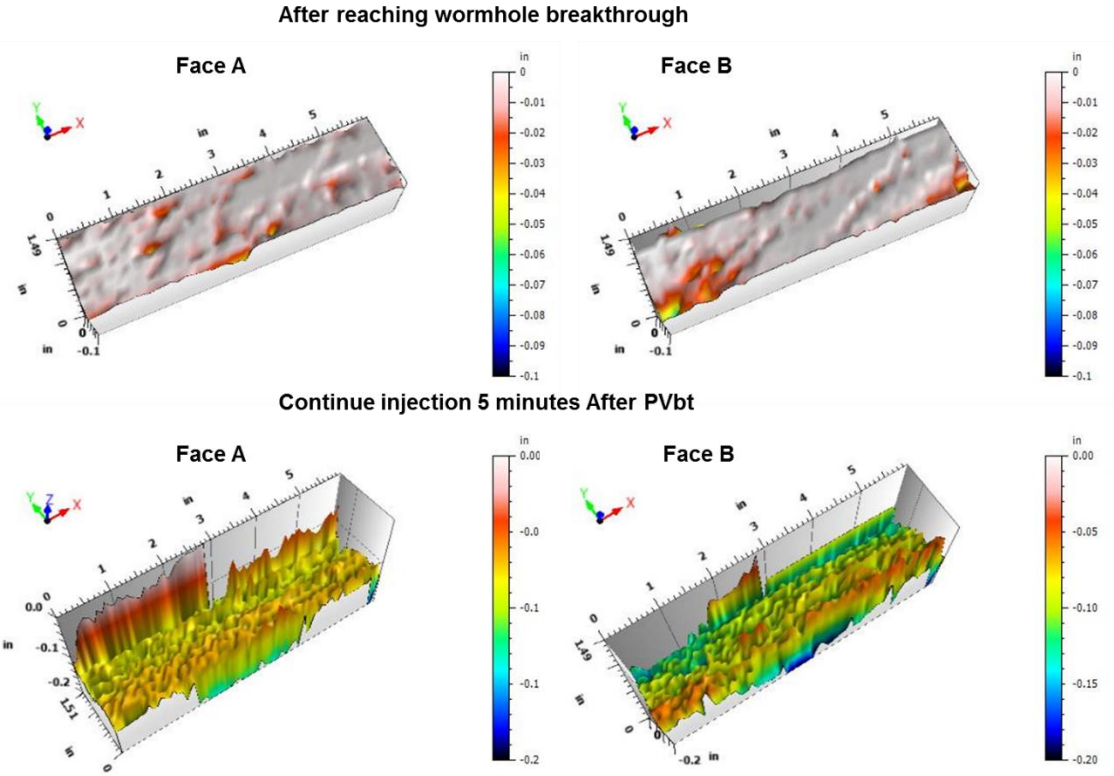

Fig. 43—Acid etching profiles of Core #21 with injection of 15 wt% HCl for 5 minutes after PVbt.

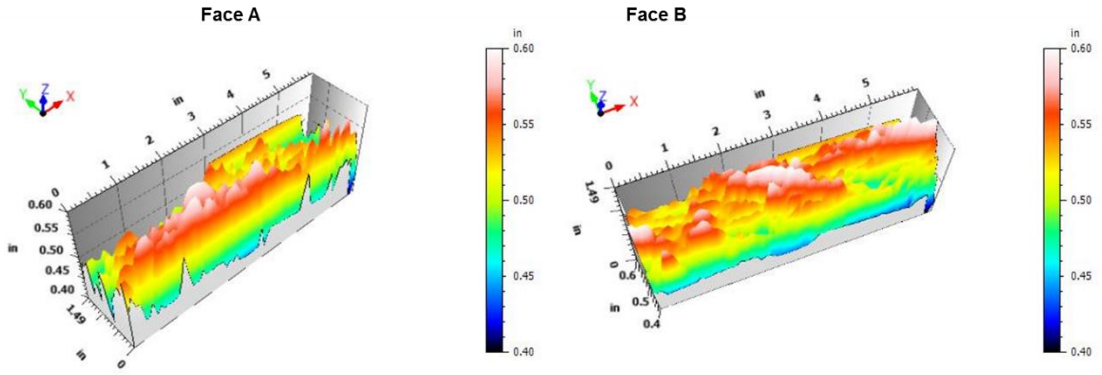

Fig. 44—Surface profiles of Core #39 with injection of 15 wt% HCl for 5 minutes after PVbt.

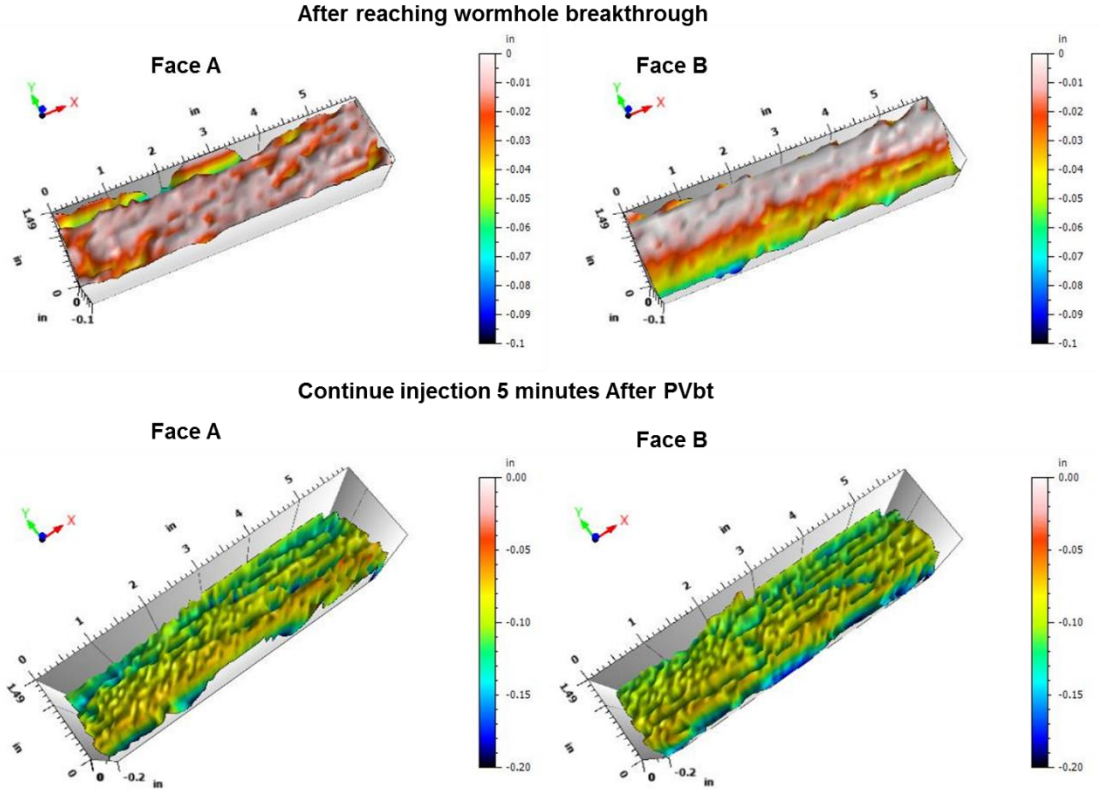

Fig. 45—Acid etching profiles of Core #39 with injection of 15 wt% HCl for 5 minutes after PVbt.

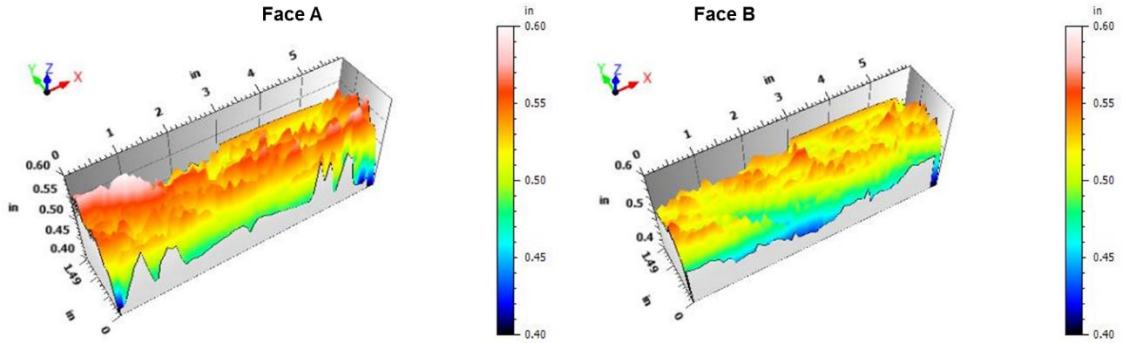

Fig. 46—Surface profiles of Core #20 with injection of 20 wt% GLDA for 30 minutes after PVbt.

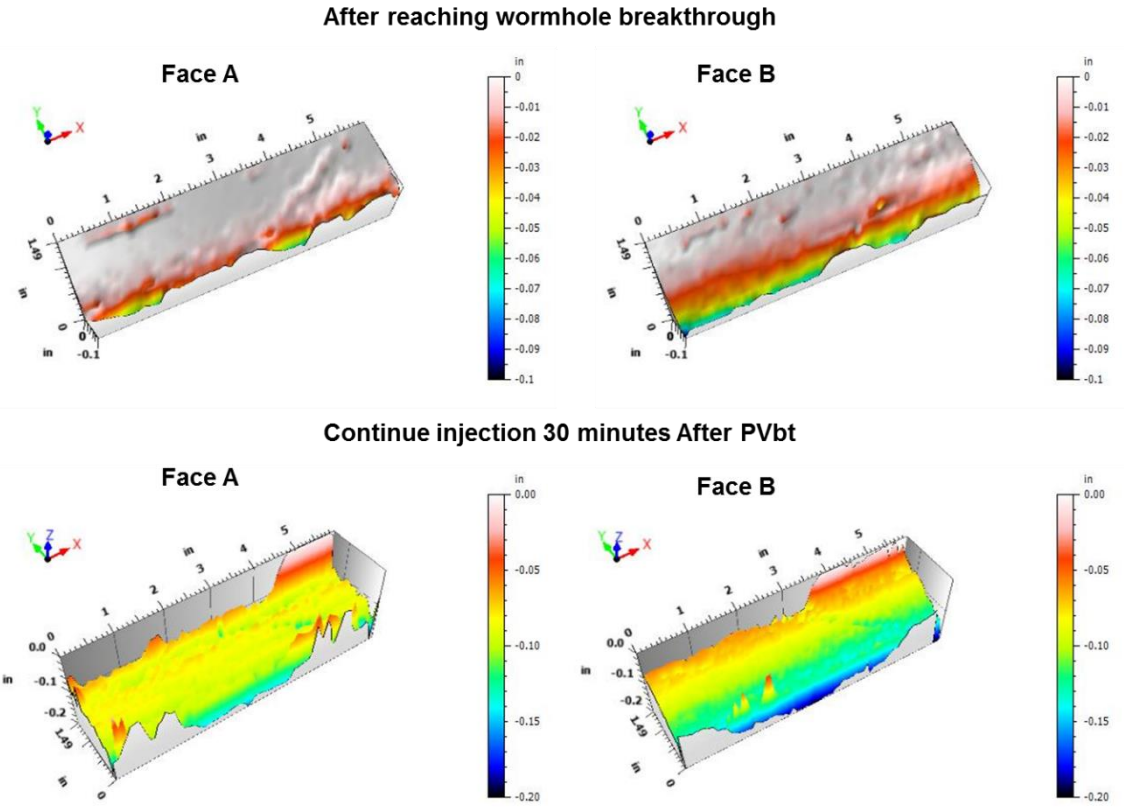

Fig. 47—Acid etching profiles of Core #20 with injection of 20 wt% GLDA for 30 minutes after PVbt.

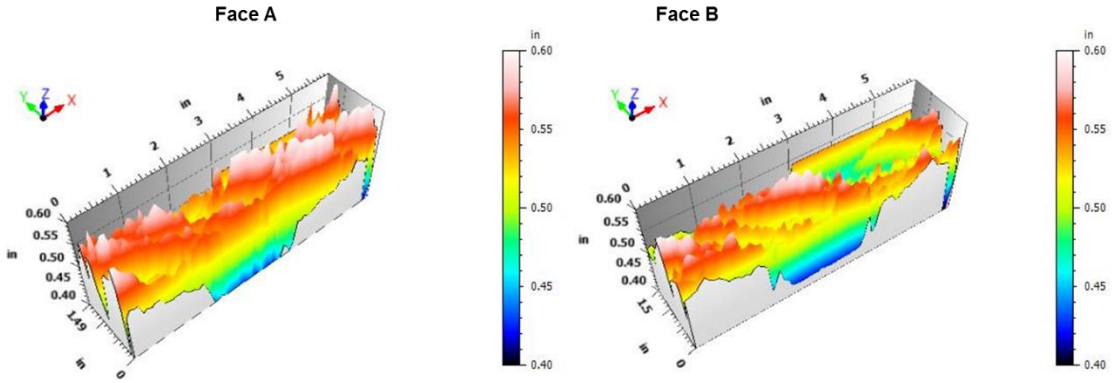

Fig. 48—Surface profiles of Core #23 with injection of 20 wt% GLDA for 30 minutes after PVbt.

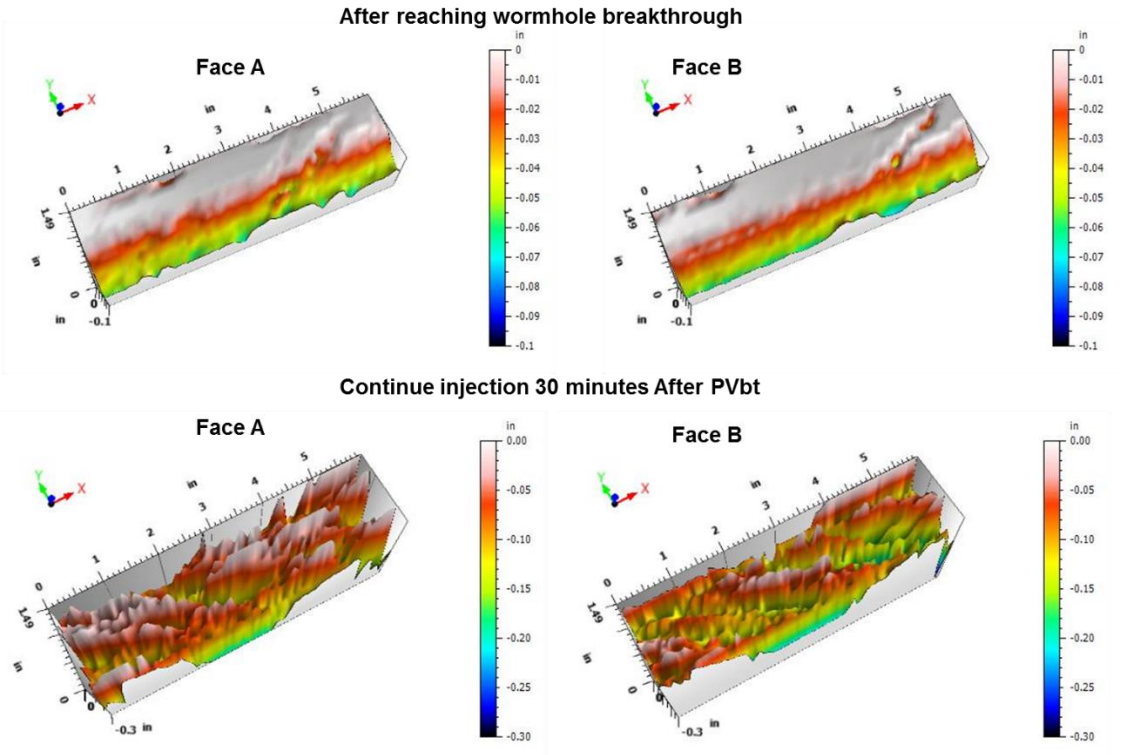

Fig. 49—Acid etching profiles of Core #23 with injection of 20 wt% GLDA for 30 minutes after PVbt.

9.4 Fracture Conductivity

For all the CFA tests with continued acid injection after PVbt, fracture conductivity was measured for all the core samples. **Fig. 49** shows the fracture conductivity measured at PVbt and continued acid injection for 5 or 30 minutes after PVbt under confining pressure of 1,500, 2,000, 3,000 and 4,000 psi conditions.

At the time of reaching wormhole breakthrough, the fracture conductivity was generally around several hundred md-ft. Table 27 already shows that the fracture conductivity was not high enough but can sustain high closure stress and maintain fracture conductivity. Wormholes or flow channels provide conductivity pathways for fluids to flow and the unreacted area can sustain high closure stress. After acid injection for 5 or 30 minutes, the fracture conductivity was substantially increased to around 10,000 md-ft for both 15 wt% HCl and 20 wt% GLDA. The values of fracture conductivity with the injection of 20 wt% GLDA are higher than fracture conductivity achieved with the injection of 15 wt% HCl.

Fig. 49 shows that all the cores maintained high fracture conductivity generated by continued acid injection under all closure stress conditions. In traditional acid fracturing treatments, fracture conductivity based on rough surfaces by differential etching can be reduced from tens of thousands to a few hundred md-ft under high closure stress conditions as most of the surfaces are closed at high closure stress. In the CFA tests proposed in this study, flow channels or wormholes are created across the fracture plane, and the unreacted areas or areas with little reaction can sustain high closure stress. Therefore, high and stable fracture conductivity is achieved.

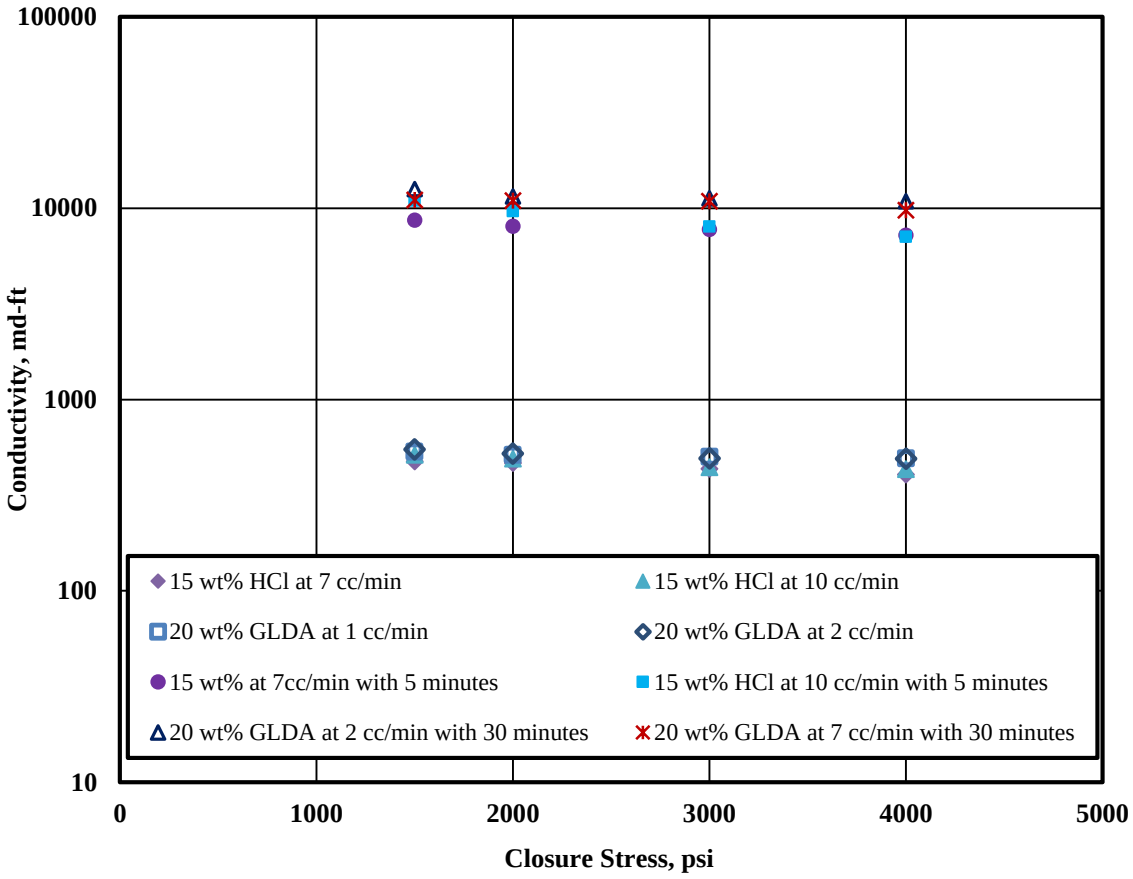

Fig. 50—Fracture conductivity at PVbt and with acid injection for some time after PVbt.

10. CONCLUSIONS AND RECOMMENDATIONS

Based on everything discussed in this study, the following conclusions can be drawn from this study:

(1) The effect of closure stress on the permeability of tensile fractures can be predicted through surface topography analysis and rock mechanical property measurements with desirable accuracy.

(2) The correlation proposed for the prediction of fracture permeability in this study contains two important parameters: the initial fracture permeability parameter that is closely related to the surface topography of tensile fractures and the change rate of fracture permeability with closure stress that can be correlated with rock embedment strength.

(3) The closure stress has a pronounced effect on fracture permeability, fracture width, and fracture porosity. Under high closure stress conditions, most of the asperities were closed. This results in limited fracture width and porosity that contribute little to the overall effective permeability of fractured cores.

(4) At 250°F, 20 wt% GLDA was more effective in creating flow channels across the fracture faces and developing long fracture lengths due to its slow reaction rate characteristics compared to 15 wt% HCl.

(5) At low acid injection rates, 15 wt% HCl created facial dissolution and caused severe rock embedment strength reduction by more than 23%. 20 wt% GLDA required less PVbt, and the rock embedment strength was reduced by less than 10%.

(6) At 250°F and 300°F, 20 wt% GLDA is more effective in creating flow channels across the fracture plane with much less acid spending rate and less damage to rock mechanical properties.

(7) With the injection of 20 wt% GLDA, more etchings on fracture faces occur at high temperature and with leakoff conditions in the radius direction, but with moderate acid spending rate.

REFERENCES

Abass, H. H., Al-Mulhem, A. A., Alqam, M. H. et al. 2006. Acid Fracturing or Proppant Fracturing in Carbonate Formation? A Rock Mechanics View. Presented at the SPE Annual Technical Conference and Exhibition, San Antonio, Texas, USA, 24-27 September. SPE-102590-MS. http://dx.doi.org/10.2118/102590-MS.

Abass, H.H., Ortiz, I., Khan, M.R. et al. 2007. Understanding Stress Dependent Permeability of Matrix, Natural Fractures, and Hydraulic Fractures in Carbonate Formations. Presented at the SPE Saudi Arabia Section Technical Symposium, Dhahran, Saudi Arabia, 7-8 May. SPE-110973-MS. http://dx.doi.org/10.2118/110973-MS.

Al-Omair, F. S. O., Siddiqui, M. A. A., Singh, J. R. et al. 2008. Fracture Acidizing of a HTHP Exploratory Well in Deep Carbonate Reservoir: A Case Study. Presented at the SPE Europe/EAGE Conference and Exhibition, Rome, Italy, 9-12 June. SPE-112794-MS. http://dx.doi.org/10.2118/112794-MS.

Anderson, M.S. and Fredrickson, S.E. 1989. Dynamic Etching Tests Aid Fracture-Acidizing Treatment Design. *SPE Prod Eng* **4** (4): 443-449. SPE-16452-PA. http://dx.doi.org/10.2118/16452-PA.

Antelo, L.F., Zhu, D., and Hill, A.D. 2009. Surface Characterization and Its Effect on Fracture Conductivity in Acid Fracturing. Presented at the SPE Hydraulic Fracturing Technology Conference, The Woodlands, Texas, 19-21 January. SPE-119743-MS. http://dx.doi.org/10.2118/119743-MS.

Aud, W. W., Wright, T. B., Cipolla, C. L. et al. 1994. The Effect of Viscosity on Near-Wellbore Tortuosity and Premature Screenouts. Presented at the SPE Annual Technical Conference and Exhibition, New Orleans, Louisiana, USA, 25-28 September. SPE-28492-MS. http://dx.doi.org/10.2118/28492-MS.

Aybar, U., Eshkalak, M.O., Sepehrnoori, K. et al. 2014. Long Term Effect of Natural Fractures Closure on Gas Production from Unconventional Reservoirs. Presented at the SPE Eastern Regional Meeting, Charleston, West Virginia, USA, 21-23 October. SPE-171010-MS. http://dx.doi.org/10.2118/171010-MS.

Bartko, K.M., Conway, M.W., Krawietz, T.E. et al. 1992. Field and Laboratory Experience in Closed Fracture Acidizing the Lisburne Field, Prudhoe Bay, Alaska. Presented at the SPE Annual Technical Conference and Exhibition, Washington, D.C., 4-7 October. SPE-24855-MS. http://dx.doi.org/10.2118/24855-MS.

Beg, M. S., Kunak, A. O., Gong, M. et al. 1998. A Systematic Experimental Study of Acid Fracture Conductivity. *SPE Prod & Fac* **13** (4): 267-271. SPE-52402-PA. http://dx.doi.org/10.2118/52402-PA.

Broaddus, G.C., and Fredrickson, S.E. 1975. Fracture Acidizing Method. US Patent No. 3,918,524.

Chacon, A. and Tiab, D. 2007. Effects of Stress on Fracture Properties of Naturally Fractured Reservoirs. Presented at the Latin American and Caribbean Petroleum Engineering Conference, Buenos Aires, Argentina, 15-18 April. SPE-107418-MS. http://dx.doi.org/10.2118/107418-MS.

Cho, Y., Ozkan, E., and Apaydin, O.G. 2013. Pressure-Dependent Natural-Fracture Permeability in Shale and Its Effect on Shale-Gas Well Production. *SPE Res Eval & Eng* **16** (2): 216-228. SPE-159801-PA. http://dx.doi.org/10.2118/159801-PA.

Cleary, M. P., Johnson, D. E., Kogsbøll, H.-H. 1993. Field Implementation of Proppant Slugs to Avoid Premature Screen-Out of Hydraulic Fractures with Adequate Proppant Concentration. Presented at the SPE Low Permeability Reservoirs Symposium, Denver, Colorado, USA, 26-28 April. SPE-25892-MS. http://dx.doi.org/10.2118/25892-MS.

Duan, Y., Jing, X., Meng, Y. et al. 2000. Closure Behaviour of Natural Rock Fractures. Presented at the SPE/AAPG Western Regional Meeting, Long Beach, California, 19-22 June. SPE-62539-MS. http://dx.doi.org/10.2118/62539-MS.

EN ISO 25178-2: 2012, Geometrical product specification (GPS) – Surface texture: Areal – Part 2: Terms, definitions and surface texture parameters. 2012.

Fredrickson, S.E. 1986. Stimulating Carbonate Formations Using a Closed Fracture Acidizing Technique. Presented at the SPE East Texas Regional Meeting, Tyler, Texas, 21-22 April. SPE-14654-MS. http://dx.doi.org/10.2118/14654-MS.

Gale, J.E. 1977. *A Numerical, Field and Laboratory Study of Flow in Rocks with Deformable Fractures*. University of California, Berkeley, California.

Garzon, F.O., Solares, J.R., Ramanathan, V. et al. 2008. Long Term Evaluation of an Innovative Acid System for Fracture Stimulation of Carbonate Reservoirs in Saudi Arabia. Presented at the International Petroleum Technology Conference, Kuala Lumpur, Malaysia, 3-5 December. SPE-12668-MS. http://dx.doi.org/10.2523/12668-MS.

Gavrilenko, P. and Gueguen, Y. 1989. Pressure Dependence of Permeability: A Model for Cracked Rocks. *Geophysical Journal International* **98** (1): 159-172. http://dx.doi.org/10.1111/j.1365-246X.1989.tb05521.x.

Gong, M., Lacote, S., and Hill, A. D. 1999. New Model of Acid-Fracture Conductivity Based on Deformation of Surface Asperities. *SPE J.* **4** (3): 206-214. SPE-57017-PA. http://dx.doi.org/10.2118/57017-PA.

Howard, G.C. and Fast, C.R. 1970. *Hydraulic Fracturing*, first edition, New York: Society of Petroleum Engineers of AIME.

Inda, A., Steffani, O., Soriano, E. et al. 2009. Field Development and Productivity Improvement in Offshore Mexico - Engineering and Laboratory Synergistic Approach to Carbonate Fracture Acidizing. Presented at the 8th European Formation Damage Conference, Scheveningen, The Netherlands, 27-29 May. SPE-121928-MS. http://dx.doi.org/ 10.2118/121928-MS.

Iwai, K. 1976. *Fundamental Studies of Fluid Flow through a Single Fracture*. Ph.D. thesis, University of California, Berkeley, California.

Jaeger, J.C. and Cook, N.G.W. 1979. *Fundamentals of Rock Mechanics*, third edition. London: Chapman and Hall.

Jahediesfanjani, H., and Civan, F. 2006. Improving Performance of the Naturally Fractured Carbonate Reservoirs by Means of the Various Stimulation and Completion Techniques. Presented at the SPE International Oil Conference and Exhibition, Cancun, Mexico, 31 August-2 September. SPE-103986-MS. http://dx.doi.org/10.2118/103986-MS.

Kalfayan, L. 2008. *Production Enhancement with Acid Stimulation*, 2nd Edition. Tulsa, Oklahoma: PennWell Corporation.

Knox, J.A., and Fredrickson, S.E. 1973. Method of Fracture Acidizing a Well Formation. US Patent No. 3,768,564.

Knox, J.A., and Fredrickson, S.E. 1974. Method of Fracture Acidizing a Well Formation. US Patent No. 3,842,911.

Kranzz, R.L., Frankel, A.D., Engelder, T. et al. 1979. The Permeability of Whole and Jointed Barre Granite. *International Journal of Rock Mechanics and Mining Sciences & Geomechanics Abstracts* **16** (4): 225-234. http://dx.doi.org/10.1016/0148-9062(79)91197-5.

LePage, J., Wolf, C.D., Bemelaar, J. et al. 2011. An Environmentally Friendly Stimulation Fluid for High-Temperature Applications. *SPE J.* **16** (1): 104-110. SPE-121709-PA. http://dx.doi.org/10.2118/121709-PA.

Liu, X., Zhao, G., Zhao, L. et al. 2003. Acid Fracturing Technique for Carbonate Reservoirs Using Nitric Acid Powder. Presented at the Canadian International Petroleum Conference, Calgary, Alberta, 10-12 June. PETSOC-2003-007. http://dx.doi.org/10.2118/2003-007.

Lynn, J. D., and Nasr-El-Din, H. A. 2001. A Core Based Comparison Of The Reaction Characteristics Of Emulsified And In-Situ Gelled Acids In Low Permeability, High Temperature, Gas Bearing Carbonates. Presented at the SPE International Symposium on Oilfield Chemistry, Houston, Texas, USA, 13-16 February. SPE-65386-MS. http://dx.doi.org/10.2118/65386-MS.

Mahmoud, M.A., Nasr-El-Din, H.A., Wolf, C.D. et al. 2011a. Evaluation of a New Environmentally Friendly Chelating Agent for High-Temperature Applications. *SPE J.* **16** (3): 559-574. SPE-127923-PA. http://dx.doi.org/10.2118/127923-PA.

Mahmoud, M.A., Nasr-El-Din, H.A., Wolf, C.D. et al. 2011b. Optimum Injection Rate of a New Chelate That Can Be Used to Stimulate Carbonate Reservoirs. *SPE J.* **16** (4): 968-980. SPE-133497-PA. http://dx.doi.org/10.2118/133497-PA.

Melendez, M.G., Pournik, M., Zhu, D. et al. 2007. The Effects of Acid Contact Time and the Resulting Weakening of the Rock Surfaces on Acid-Fracture Conductivity. Presented at the European Formation Damage Conference, Scheveningen, The Netherlands, 30 May-1 June. SPE-107772-MS. http://dx.doi.org/10.2118/107772-MS.

Nasr-El-Din, H. A., Solares, J. R., Al-Mutairi, S. H. et al. 2001. Field Application of Emulsified Acid-Based System to Stimulate Deep, Sour Gas Reservoirs in Saudi Arabia. Presented at the SPE Annual Technical Conference and Exhibition, New Orleans, Louisiana, USA, 30 September-3 October. SPE-71693-MS. http://dx.doi.org/10.2118/71693-MS.

Nasr-El-Din, H. A., Al-Mutairi, S., Al-Malki, B. et al. 2002a. Stimulation of Deep Gas Wells Using HCl/Formic Acid System: Lab Studies and Field Application. Presented at the Canadian International Petroleum Conference, Calgary, Alberta, 11-13 June. PETSOC-2002-289. http://dx.doi.org/10.2118/2002-289.

Nasr-El-Din, H. A., Taylor, K. C., and Al-Hajji, H. H. 2002b. Propagation of Cross-linkers Used in In-Situ Gelled Acids in Carbonate Reservoirs. Presented at the SPE/DOE Improved Oil Recovery Symposium, Tulsa, Oklahoma, USA, 13-17 April. SPE-75257-MS. http://dx.doi.org/10.2118/75257-MS.

Nasr-El-Din, H. A., Al-Driweesh, S., Al-Muntasheri, G. A. et al. 2003. Acid Fracturing HT/HP Gas Wells Using a Novel Surfactant Based Fluid System. Presented at the SPE Annual Technical Conference and Exhibition, Denver, Colorado, USA, 5-8 October. SPE-84516-MS. http://dx.doi.org/10.2118/84516-MS.

Nasr-El-Din, H. A., Al-Driweesh, S. M., Bartko, K. M. et al. 2006a. Acid Fracturing of Deep Gas Wells Using a Surfactant-Based Acid: Long-Term Effects on Gas Production Rate. Presented at the SPE Annual Technical Conference and Exhibition, San Antonio, Texas, USA, 24-27 September. SPE-102469-MS. http://dx.doi.org/10.2118/102469-MS.

Nasr-El-Din, H. A., Al-Driweesh, S. M., Sierra, L. et al. 2006b. First Field Application of In-Situ Gelled HCl-Formic Acid System. Presented at the International Oil Conference and Exhibition, Cancun, Mexico, 31 August-2 September. SPE-103978-MS. http://dx.doi.org/10.2118/103978-MS.

Nasr-El-Din, H. A., Al-Driweesh, S. M., Chesson, J. B. et al. 2008. Fracture Acidizing: What Role Does Formation Softening Play in Production Response? *SPE Prod & Oper* **23** (2): 184-191. SPE-103344-PA. http://dx.doi.org/10.2118/103344-PA.

Nasr-El-Din, H. A., Solares, J. R., Al-Zahrani, A. A. et al. 2009. Acid Fracturing of Gas Wells Using Solid Acid: Lessons Learned From First Field Application. *SPE Prod & Oper* **24** (2): 320-335. SPE-110895-PA. http://dx.doi.org/10.2118/110895-PA.

Nasr-El-Din, H.A., Solares, J.R., Al-Zahrani, A.A. et al. 2007. Acid Fracturing of Gas Wells Using Solid Acid: Lessons Learned from First Field Application. Presented at the SPE Annual Technical Conference and Exhibition, Anaheim, California, 11-14 November. SPE-110895-MS. http://dx.doi.org/10.2118/110895-MS.

Nierode, D. E., and Kruk, K. F. 1973. An Evaluation of Acid Fluid Loss Additives Retarded Acids, and Acidized Fracture Conductivity. Presented at the Fall Meeting of the Society of Petroleum Engineers of AIME, Las Vegas, Nevada, USA, 30 September-3 October. SPE-4549-MS. http://dx.doi.org/10.2118/4549-MS.

Nieto, C.M., Pournik, M., and Hill, A.D. 2008. The Texture of Acidized Fracture Surfaces: Implications for Acid Fracture Conductivity. *SPE Prod & Oper* **23** (3):343 - 352. SPE-102167-PA. http://dx.doi.org/10.2118/102167-PA.

Nnanna, E. J., and Ajienka, J. A. 2005. Critical Success Factors for Well Stimulation. Presented at the SPE Nigeria Annual International Conference and Exhibition, Abuja, Nigeria, 1-3 August. SPE-98823-MS. http://dx.doi.org/10.2118/98823-MS.

Ozkan, E., Raghavan, R.S., and Apaydin, O.G. 2010. Modeling of Fluid Transfer from Shale Matrix to Fracture Network. Presented at the SPE Annual Technical Conference

and Exhibition, Florence, Italy, 19-22 September. SPE-134830-MS. http://dx.doi.org/10.2118/134830-MS.

Patzek, T.W., Male, F., and Marder, M. 2013. Gas Production in the Barnett Shale Obeys a Simple Scaling Theory. *Proceedings of the National Academy of Sciences* **110** (49): 19731-19736. http://dx.doi.org/10.1073/pnas.1313380110.

Pournik, M., Nasr-El-Din, H.A., and Mahmoud, M.A. 2011. A Novel Application of Closed-Fracture Acidizing. *SPE Prod & Oper*, **26** (1):18-29. SPE-124874-PA. http://dx.doi.org/10.2118/124874-PA.

Pournik, M., Zou, C., Malagon Nieto, C. et al. 2007. Small-Scale Fracture Conductivity Created by Modern Acid-Fracture Fluids. Presented at the SPE Hydraulic Fracturing Technology Conference, College Station, Texas, USA, 29-31 January. SPE-106272-MS. http://dx.doi.org/10.2118/106272-MS.

Pournik, M., Gomaa, A.M., and Nasr-El-Din, H.A. 2010a. Influence of Acid-Fracture Fluid Properties on Acid-Etched Surfaces and Resulting Fracture Conductivity. Presented at the SPE International Symposium and Exhibition on Formation Damage Control, Lafayette, Louisiana, USA, 10-12 February. SPE-128070-MS. http://dx.doi.org/10.2118/128070-MS.

Pournik, M., Li, L., Smith, B. et al. 2010b. Effect of Acid Spending on Etching and Acid Fracture Conductivity (Russian). Presented at the SPE Russian Oil and Gas Conference and Exhibition, Moscow, Russia, 26-28 October. SPE-136217-RU. http://dx.doi.org/10.2118/136217-RU.

Pournik, M. and Nasr-El-Din, H.A. 2010c. Laboratory Evaluation of Acid Refracturing Performance. Presented at the SPE Latin American and Caribbean Petroleum Engineering Conference, Lima, Peru, 1-3 December. SPE-138623-MS. http://dx.doi.org/10.2118/138623-MS.

Pournik, M. 2008. *Laboratory-Scale Fracture Conductivity Created by Acid Etching*. Ph.D. thesis, Texas A&M University, College Station, Texas.

Rabie, A.I, Mahmoud, M.A, and Nasr-El-Din, H.A. 2011. Reaction of GLDA with calcite: Reaction Kinetics and Transport Study. Presented at the SPE International Symposium on Oilfield Chemistry, The Woodlands, Texas, USA, 11-13 April. SPE-139816-MS. http://dx.doi.org/10.2118/139816-MS.

Raghavan, R. and Chin, L.Y. 2002. Productivity Changes in Reservoirs with Stress-Dependent Permeability. Presented at the SPE Annual Technical Conference and Exhibition, San Antonio, Texas, 29 September-2 October. SPE-77535-MS. http://dx.doi.org/10.2118/77535-MS.

Raysoni, N., and Weaver, J. D. 2012. Long-Term Proppant Performance. Presented at the SPE International Symposium and Exhibition on Formation Damage Control, Lafayette, Louisiana, USA, 15-17 February. SPE-150669-MS. http://dx.doi.org/10.2118/150669-MS.

Rodrigues, V.F., Campos, W., Medeiros, A.C. et al. 2011. Acid-Fracture Conductivity Correlations for a Specific Limestone Based on Surface Characterization. Presented at the SPE Annual Technical Conference and Exhibition, Denver, Colorado, USA, 30 October-2 November. SPE-145298-MS. http://dx.doi.org/10.2118/145298-MS.

Ruffet, C., Fery, J.J., and Onaisi, A. 1998. Acid Fracturing Treatment: A Surface Topography Analysis of Acid Etched Fractures to Determine Residual Conductivity. *SPE J.* **3** (2):155-162. SPE-38175-PA. http://dx.doi.org/10.2118/38175-PA.

Sarna, A., Xing, Q., Mork, J. et al. 2014. Impact of Fracture Closure on Productivity Decline of Unconventional Wells. Presented at the SPE Western North American and Rocky Mountain Joint Meeting, Denver, Colorado, 17-18 April. SPE-169590-MS. http://dx.doi.org/10.2118/169590-MS.

Sizer, J.P., Moullem, A.S., and Abou-Sayed, I.S. 1991. Evaluation of Closed Fracture Acidizing Performed in a Tight Limestone Formation. Presented at the Middle East Oil Show, Bahrain, 16-19 November. SPE-21440-MS. http://dx.doi.org/10.2118/21440-MS.

Torcuk, M.A., Kurtoglu, B., Fakcharoenphol, P. et al. 2013. Theory and Application of Pressure and Rate Transient Analysis in Unconventional Reservoirs. Presented at the SPE Annual Technical Conference and Exhibition, New Orleans, Louisiana, USA, 30 September-2 October. SPE-166147-MS. http://dx.doi.org/10.2118/166147-MS.

Taylor, K. C., and Nasr-El-Din, H. A. 2001. Laboratory Evaluation of In-Situ Gelled Acids for Carbonate Reservoirs. Presented at the SPE Annual Technical Conference and Exhibition, New Orleans, Louisiana, USA, 30 September-3 October. SPE-71694-MS. http://dx.doi.org/10.2118/71694-MS.

Taylor, K. C., and Nasr-El-Din, H. A. 2002. Coreflood Evaluation of In-Situ Gelled Acids. Presented at the International Symposium and Exhibition on Formation Damage Control, Lafayette, Louisiana, 20-21 February. SPE-73707-MS. http://dx.doi.org/10.2118/73707-MS.

Trimmer, D., Bonner, B., Heard, H.C. et al. 1980. Effect of Pressure and Stress on Water Transport in Intact and Fractured Gabbro and Granite. *Journal of Geophysical Research* **85** (B12): 7059-7071.

Tsang, Y.W. and Witherspoon, P.A. 1981. Hydromechanical Behavior of a Deformable Rock Fracture Subject to Normal Stress. *Journal of Geophysical Research: Solid Earth* **86** (B10): 9287-9298. http://dx.doi.org/10.1029/JB086iB10p09287.

Van Batenburg, D., Biezen, E., and Weaver, J. 1999. Towards Proppant Back-Production Prediction. Presented at the SPE European Formation Damage Conference, The Hague, The Netherlands, 31 May-1 June. SPE-54730-MS. http://dx.doi.org/10.2118/54730-MS.

Van Dam, D.B., de Pater, C.J., and Romijn, R. 2000. Analysis of Hydraulic Fracture Closure in Laboratory Experiments. *SPE Prod & Fac* **15** (3): 151-158. SPE-65066-PA. http://dx.doi.org/10.2118/65066-PA.

Van Dam, D.B., Papanastasiou, P., and de Pater, C.J. 2002. Impact of Rock Plasticity on Hydraulic Fracture Propagation and Closure. *SPE Prod & Fac* **17** (3):149-159. SPE-78812-PA. http://dx.doi.org/10.2118/78812-PA.

Vega Navarro, O.G. 2012. Closure of Natural Fractures Caused by Increased Effective Stress, a Case Study: Reservoir Robore III, Bulo Bulo Field, Bolivia. Presented at the SPE Latin America and Caribbean Petroleum Engineering Conference, Mexico City, Mexico, 16-18 April. SPE 153609-MS. http://dx.doi.org/10.2118/153609-MS.

Walsh, J.B. 1981. Effect of Pore Pressure and Confining Pressure on Fracture Permeability. *International Journal of Rock Mechanics and Mining Sciences & Geomechanics Abstracts* **18** (5): 429-435. http://dx.doi.org/10.1016/0148-9062(81)90006-1.

Wang, X., Zou, H., Zheng, X. et al. 2003. Optimization of Acid Fracturing to Improve Heavy Oil Production in Naturally Fractured Carbonates. Presented at the SPE Production and Operations Symposium, Oklahoma, 23-26 March. SPE-80897-MS. http://dx.doi.org/10.2118/80897-MS.